Cell Stem Cell

Resource

Spatially patterned kidney assembloids recapitulate progenitor self-assembly and enable high-fidelity *in vivo* disease modeling

Graphical abstract

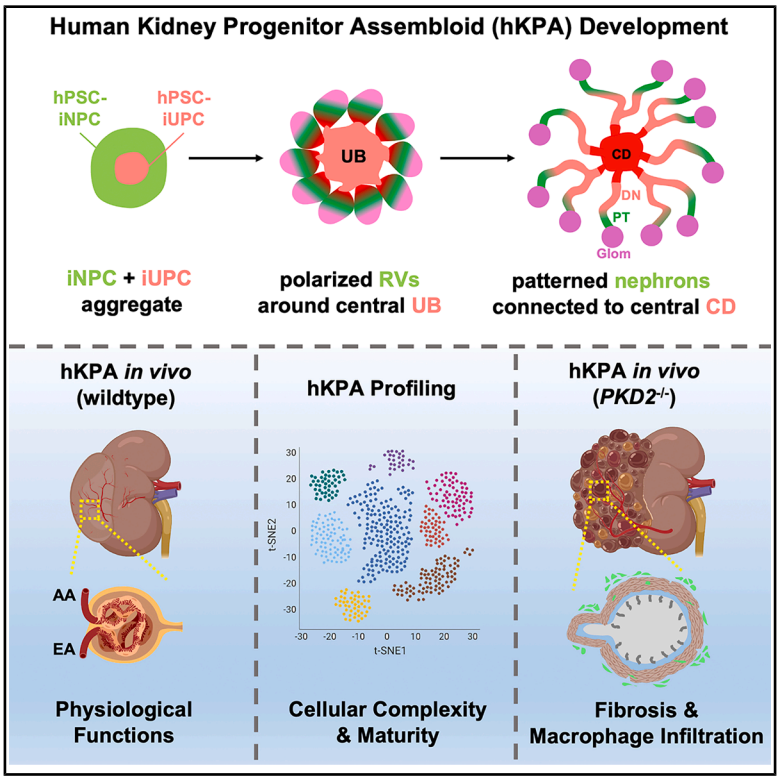

Highlights

- Human kidney progenitor assembloid (hKPA) develops from hPSC-derived iNPCs and iUPCs
- hKPA shows polarized RVs from iNPCs around a central iUPC-derived UB
- Patterned nephrons fuse with the central CD and display kidney-like functions
- *In vivo*-grown *PKD2*$^{-/-}$ hKPA models complex pathogenic cell-cell interactions

Authors

Biao Huang, Pedro Medina, Jincan He, ..., Cizhong Jiang, Andrew P. McMahon, Zhongwei Li

Correspondence

zhongwei.li@med.usc.edu

In brief

Recapitulating the self-assembly of kidney progenitors, Huang, Medina, He, Zeng, and colleagues have developed mouse and human kidney progenitor assembloids, exhibiting enhanced cellular complexity, spatial organization, maturation, and functional capacity. These sophisticated models provide high-fidelity platforms for disease modeling and establish a robust foundation for kidney regenerative medicine.

Huang et al., 2025, Cell Stem Cell *32*, 1614–1633
October 2, 2025
https://doi.org/10.1016/j.stem.2025.08.013

CellPress

CellPress

Cell Stem Cell

Resource

Spatially patterned kidney assembloids recapitulate progenitor self-assembly and enable high-fidelity *in vivo* disease modeling

Biao Huang,[1,2,11] Pedro Medina,[1,2,11] Jincan He,[3,11] Zipeng Zeng,[1,2,11] Sunghyun Kim,[2] Janet Romo,[2] Kari Koppitch,[2] Chennan C. Zhang,[1,2] Georgina Gyarmati,[4] Yohan Park,[5] Ruslan Bohovyk,[6] Pierre-Emmanuel Yoann N'Guetta,[7] Jinjin Guo,[2] Tianyi Ma,[1,2] Megan E. Schreiber,[1,2] Cong Xu,[1,2] Jessica Pham,[1] Riana K. Parvez,[2] Jackson Su,[1,2] Mateo W. Xia,[1,2] Zhenqing Liu,[8] Laura Perin,[9] Danny El-Nachef,[2] Charles E. Murry,[2] Sanjeev Kumar,[10] Lori O'Brien,[7] Kurt A. Zimmerman,[5] Justin Ichida,[2] Nils O. Lindström,[2] Nuria M. Pastor-Soler,[1] Kenneth R. Hallows,[1] Alexander Staruschenko,[6] Janos Peti-Peterdi,[4] Cizhong Jiang,[3] Andrew P. McMahon,[2] and Zhongwei Li[1,2,12,*]

[1]Vito M. Campese MD/UKRO Kidney Research Center, Division of Nephrology and Hypertension, Department of Medicine, Keck School of Medicine, University of Southern California, Los Angeles, CA 90033, USA

[2]Department of Stem Cell Biology and Regenerative Medicine, Keck School of Medicine, University of Southern California, Los Angeles, CA 90033, USA

[3]Key Laboratory of Spine and Spinal Cord Injury Repair and Regeneration of Ministry of Education, Orthopaedic Department of Tongji Hospital, School of Life Sciences and Technology, Tongji University, Shanghai 200065, China

[4]Department of Physiology and Neuroscience and Department of Medicine, Zilkha Neurogenetic Institute, University of Southern California, Los Angeles, CA 90033, USA

[5]Department of Internal Medicine, Division of Nephrology and Hypertension, University of Oklahoma Health Sciences Center, Oklahoma City, OK 73034, USA

[6]Department of Molecular Pharmacology and Physiology, University of South Florida, Tampa, FL 33602, USA

[7]Department of Cell Biology and Physiology, The University of North Carolina at Chapel Hill, Chapel Hill, NC 27599, USA

[8]Department of Neurodegenerative Diseases, Beckman Research Institute of City of Hope, Duarte, CA 91010, USA

[9]GOFARR Laboratory, Division of Urology, Saban Research Institute, Children's Hospital Los Angeles, Los Angeles, CA 90027, USA

[10]Board of Governors Regenerative Medicine Institute, Cedars-Sinai Medical Center, Los Angeles, CA 90048, USA

[11]These authors contributed equally

[12]Lead contact

*Correspondence: zhongwei.li@med.usc.edu

https://doi.org/10.1016/j.stem.2025.08.013

SUMMARY

Current kidney organoids do not recapitulate the kidney's complex spatial patterning and function, limiting their applications. The human kidney comprises one million nephrons, derived from nephron progenitor cells, that connect to an arborized ureteric progenitor cell-derived collecting system. Here, we develop spatially organized mouse and human kidney progenitor assembloid (KPA) models in which the nephrons undergo extensive development and fuse to a centrally located collecting system, recapitulating kidney progenitor self-assembly processes observed *in vivo*. KPAs show dramatically improved cellular complexity and maturity and exhibit several aspects of major kidney functions *in vitro* and *in vivo*. Modeling human autosomal dominant polycystic kidney disease (ADPKD) with genome-edited, *in vivo*-grown human KPAs recapitulated the cystic phenotype and the molecular and cellular hallmarks of the disease and highlighted the crosstalk among cyst epithelium, stroma, and macrophages. The KPA platform opens new avenues for high-fidelity disease modeling and lays a strong foundation for kidney regenerative medicine.

INTRODUCTION

One in seven adults develops kidney diseases, but limited progress has been made to develop novel therapeutics. One major roadblock is the lack of a physiologically relevant human kidney model. Human pluripotent stem cell (hPSC)-derived kidney organoids offer a promising patient-specific, three-dimensional complex human kidney model for kidney research.[1–15] However, despite the progress over the past decade, current kidney organoid models still do not recapitulate the kidney's complex spatial patterning, are immature, are equivalent to an embryonic kidney,[16–19] and fail to recapitulate major physiological functions of the kidney. With these major limitations, they are not generally accurate in modeling human kidney diseases, most of which are late-onset with impaired kidney physiological functions. Immaturity and lack of functionality also prevent the development of functional kidney tissues for regenerative medicine.

The mammalian kidney has over 30 cell types differentiated at discrete positions along the length of the continuous kidney tubular network, performing a variety of physiological functions.[20–22] Despite the complexity, the kidney is self-assembled in the embryo from repetitive interactions among a few types of kidney progenitor cells.[23,24] Of these, reciprocal interactions between the SIX2$^+$ nephron progenitor cells (NPCs)[25] and the WNT11$^+$ ureteric progenitor cells (UPCs)[26] lay the foundation of kidney organogenesis: NPCs generate nephrons, the functional units of the kidney, which filter the blood, produce urine, and refine urine components,[27] and UPCs give rise to the ureteric bud (UB), which branches and differentiates to form the collecting duct (CD) network, which balances water, salt, and pH of the body fluids and transports urine via the ureter to the bladder.[28] In addition, FOXD1$^+$ interstitial progenitor cells (IPCs) form the kidney's diverse stromal populations,[29] while vascular progenitor cells (VPCs) build the kidney's blood vessels.[30]

As different kidney progenitor cell types form from distinct spatial and temporal origins[23,24] that cannot be readily recapitulated in a single protocol, we[6,11,14] and others[1,2,4,5,7,15,31–34] have developed separate protocols to generate transient NPCs or UPCs from PSCs or derive expandable NPC or UPC lines from primary cells or PSCs. These NPCs or UPCs can further differentiate into nephron[1,2,4–11] or CD[3,12–15] organoids, respectively. However, these kidney organoids are immature, can only model part of the kidney (nephron or CD), and do not recapitulate the elaborate spatial patterning of the kidney essential for its function.[16–19]

Toward the assembly of a more structurally complex kidney organoid model, we[6,11,14] and others[33,35,36] have shown that mixing of different types of native or *in vitro*-generated mouse kidney progenitor cells that are either expanded from primary kidney progenitor cells or derived from mouse PSCs leads to spontaneous generation of early mouse embryonic kidney-like structures. However, these structures are also immature and therefore lack critical kidney functions. Functional human kidney organoids with elaborate spatial patterning of nephrons and CD have not been generated from human PSCs, despite some recent attempts mixing human PSC-derived kidney progenitor cells.[13,37–41]

Here, we systematically optimized kidney development *in vitro* and applied these conditions to kidney progenitor cultures to enable the self-assembly of mouse and human kidney progenitor assembloids (KPAs) with spatially organized nephrons and a central CD system and with improved maturity and demonstrated functionality *in vitro* and *in vivo*. Modeling polycystic kidney disease using genome-edited, *in vivo*-grown human KPAs (hKPAs) showcased the platform's exceptional potential for faithfully recapitulating complex human kidney diseases.

RESULTS

Assembly of a mouse KPA from expandable NPCs and UPCs

Current mouse kidney organoids[33,35,36] or explant culture of embryonic day 11.5–12.5 (E11.5–E12.5) mouse kidneys[42] undergo a developmental process mirroring *in vivo* development but cease to develop after reaching a developmental stage equivalent to an E15.5 kidney, resulting in immature kidney tissue *in vitro*. We reasoned that a culture condition enabling *in vitro* kidney development beyond E15.5 will be essential to develop mature and functional kidney organoid models. Thus, we first systematically optimized mouse kidney explant culture (Methods S1; Mendeley Data Figure S1; STAR Methods). The identified stepwise "v2 medium" culture system supports the *in vitro* maturation from an embryonic kidney to a postnatal kidney stage, developing spatially organized nephrons, CD, stroma, and ureter (Figure S1; Methods S2; Videos S1 and S2; Mendeley Data Figure S2; STAR Methods).

Co-development of *in vitro*-expanded *Six2*-GFP$^+$ mouse NPCs[11] and *Hoxb7*-Venus$^+$ mouse UPCs[14] in v2 medium generated a highly spatially organized kidney structure, referred to hereafter as "mouse KPA" or "mKPA" (Figures 1A–1C, S2A, and S2B; Methods S2–S4; Video S3). *Hoxb7*-Venus$^+$ UPCs spontaneously clustered in the center of the NPC/UPC aggregates, invaded, and branched into the surrounding NPCs to form the UB (Figure 1B, left), which further branched and generated a tree-like central UB/CD network (Figures 1B, right, 1C, and S2B–S2D). The first UB bifurcation was observed on day 2, in which the SIX2$^+$ NPCs condensed around the bifurcating KRT8$^+$ UB tips, reconstituting the nephrogenic niche (Figure 1D). Thereafter, SIX2$^+$/WT1$^+$ NPCs were found to cap the UB tips and retain the nephrogenic niche, while a subset of NPCs was induced to form renal vesicle (RV) and S-shaped body (SSB) around the UB trunk region, representing the initiation of nephrogenesis (Figures 1E and S2E). After about 3 weeks, mKPAs were fully developed, generating around 150 nephrons, as estimated by the number of round PODXL$^+$/WT1$^+$ glomerulus-like structures observed (Figures 1F, S2F, and S2G). Of these nephrons, different segments of the nephron tubules were specified, including LTL$^+$/LRP2$^+$/HNF4A$^+$ proximal tubule (PT), AQP1$^+$ descending limb of loop of Henle (dLOH), SLC12A1$^+$/UMOD$^+$ ascending limb of loop of Henle (aLOH), and POU3F3$^+$/GATA3$^+$/CDH1$^+$ distal nephron (DN) (Figures 1G and S2I–S2M). The GATA3$^+$/CDH1$^+$/*Hoxb7*-Venus$^-$ distal end of the nephron tubule connected with the GATA3$^+$/CDH1$^+$/*Hoxb7*-Venus$^+$ UPC-derived CD, suggesting connecting tubule (CNT) formation (Figures 1H and S2H). In the UPC-derived CD, AQP2$^+$ principal cells (PCs) and FOXI1$^+$/ATP6V1B1$^+$ intercalated cells (ICs) were both generated, with spatial organization and abundance similar to that found in a native postnatal kidney (Figures S2N–S2P). Primary cilia were identified facing the lumen side of the tubules (Figure S2Q). Unexpectedly, diverse kidney stromal populations, progenies of the FOXD1$^+$ IPCs,[29] were identified and exhibited discrete spatial locations in the mKPAs: MEIS1/2/3$^+$/PDGFRB$^+$ interstitial cells in the space between and surrounding nephrons and CD (Figures 1I and 1K), PDGFRB$^+$/DESMIN$^+$/ACTA2$^-$/WT1$^-$ mesangial cells (MCs) in the round glomerulus-like structures (Figures S3A–S3C), ACTA2$^+$ smooth muscle cells surrounding the central CD (Figures 1J and S3C), and PDGFRB$^+$/LIV2$^+$ renal capsule cells at the periphery (Figure S3D). *Igfbp6*, *Alx1*, and *Penk*, demarcating specific stromal cell populations along the cortical-medullary axis,[43] were visualized by RNAscope *in situ* hybridization in the mKPAs (Figures S3E–S3K). Interestingly, as early as day 1, a layer of FOXD1$^+$ IPCs was observed on the periphery of the mKPAs, surrounding SIX2$^+$ NPCs (Figure 1L). On day 2, upon the first UB branching and condensation of NPCs around UB tips, FOXD1$^+$ IPCs were located close to the NPCs, forming a

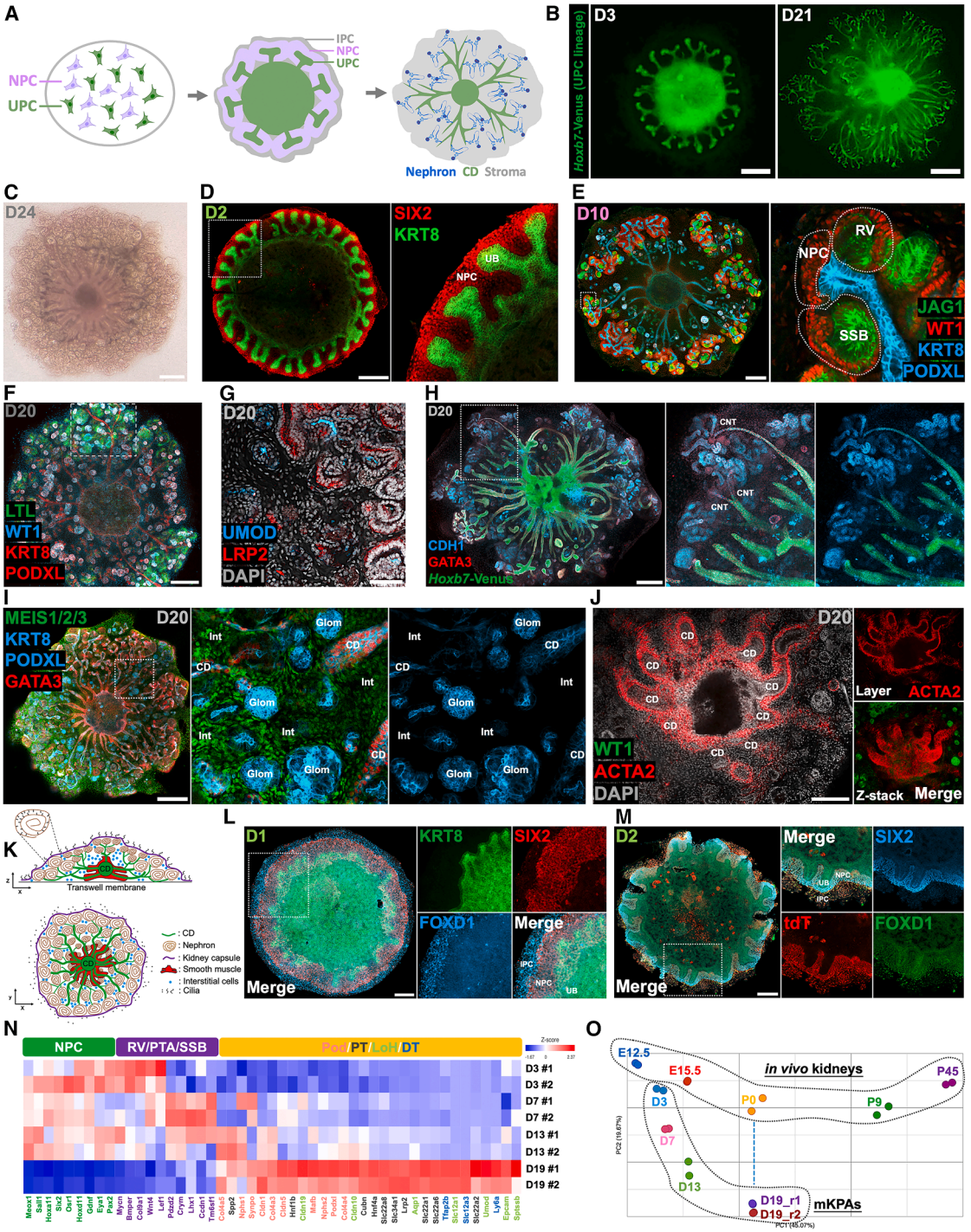

Figure 1. Assembly of an mKPA from expandable NPCs and UPCs

(A) Schematic of mKPA development.

(B) *Hoxb7*-Venus fluorescence images of mKPAs on days 3 and 21. Scale bars, 200 μm.

(C) Bright-field (BF) image of a day 24 mKPA. Scale bar, 500 μm.

(D–J) Whole-mount immunofluorescence images of mKPAs. Enlarged picture of the white boxed area in (F) is shown in Figure S2F. Scale bars, 200 μm (D, E, and J), 500 μm (F, H, and I), and 50 μm (G).

(K) Schematic of the spatial organization of mKPA.

(L and M) Whole-mount immunofluorescence images of day 1 (L) and day 2 (M) mKPAs. Scale bar, 200 μm.

(N) Heatmap showing the expression of marker genes from bulk RNA-seq datasets.

(O) PCA of bulk RNA-seq datasets comparing time course mKPA development *in vitro* with kidney development *in vivo* from E12.5 to postnatal day 45 (P45).

See also Figures S1–S4.

complete nephrogenic niche with three types of progenitor cells spatially organized as in a native developing kidney (Figures S3L and S3M). Lineage-tracing of NPCs and derivatives with *Six2*-tdTomato (*Six2*-tdT) reporter[20,25] indicated the NPC origin of these IPCs, as well as the more differentiated MEIS1/2/3$^+$/PDGFRB$^+$ interstitial cells (Figures 1M and S3N–S3P). These results suggest NPC-to-IPC transdifferentiation as a source for the formation of diverse stromal populations in the mKPAs.

Transcriptome analysis with bulk RNA sequencing (RNA-seq) indicates mKPA development *in vitro* recapitulated major molecular events of nephrogenesis (Figure 1N; Table S1) and CD differentiation (Figure S4A; Table S1). It also confirmed the expression of stromal genes and showed temporal elevation of IPC marker genes in the early mKPAs (Figure S4B; Table S1). Principal-component analysis (PCA) indicates the transcriptome of mKPA at the endpoint of *in vitro* development resembles a postnatal kidney (Figure 1O; Table S1). Supporting this, *AQP1*, *UMOD*, and other selected genes that are expressed in postnatal mouse kidneys[44] are expressed in the mKPAs (Figures 1G, S2L, and S4C–S4E; Methods S5).

Single-cell multiome analyses of mKPAs

We next employed single-nuclear multiome analysis (single-nucleus RNA-seq [snRNA-seq] + single-nucleus assay for transposase-accessible chromatin using sequencing [snATAC-seq]) on day 24 mKPAs. tdT (*Six2*-tdT$^+$)[20,25] and Venus (*Hoxb7*-Venus$^+$)[45] lineage reporters distinguished NPC and UPC descendant cell types, respectively (Figure 2A). Consistent with our bulk RNA-seq and immunostaining results, unsupervised clustering of the snRNA-seq dataset identified nephron, ureteric epithelium, proliferative cells, and a diverse stromal/interstitial population arising from NPCs (tdT$^+$; Figure 2B; Tables S1 and S2). Subclustering of the nephron and ureteric epithelium populations identified NPC and major segments of the nephron, including podocyte (Pod), parietal epithelial cells (PECs), PT, LOH, and distal tubule (DT), as well as UPC, PC, and IC of the ureteric epithelium (Figures 2C and 2D; Table S2). In addition, snRNA-seq and snATAC-seq suggested a diverse interstitial population representing cortical, medullary, and CD stromal cell populations as identified *in vivo*[46] (Mendeley Data Figures S3A–S3F).

To directly compare mKPAs with native postnatal mouse kidneys, we integrated our snRNA-seq and snATAC-seq with recently published datasets of postnatal day 0 (P0) mouse kidneys.[47] As expected, mKPAs closely resemble P0 kidney cellular components (Figures 2E and 2F; Mendeley Data Figures S3G–S3I). Subclustering DN and CD clusters confirmed the observed nephron/CD connection, showing a gradual transition from proximal to distal cell profiles, including *tdT*$^+$/*Hoxd10*$^+$/*Slc12a1*$^+$ LOH, *tdT*$^+$/*Hoxd10*$^+$/*Slc12a3*$^+$ distal convoluted tubule (DCT), *tdT*$^+$/*Hoxd10*$^+$/*Gata3*$^+$/*Aqp2*$^+$ CNT, and *Venus*$^+$/*Hoxd10*$^-$/*Gata3*$^+$/*Aqp2*$^+$ PC (Figure 2G). Importantly, multiple genes, including *Umod*, *Slc12a3*, *Col4a3*, and *Col4a4*, that demarcate advanced stages of kidney development consistent with P0 kidney comparison, showed an active chromatin accessibility profile and were expressed in the mKPAs (Figures 2H–2K).

Functional maturation of mKPAs *in vitro* and *in vivo*

Bulk RNA-seq and single-cell multiome analyses of mKPAs indicated key genes mediating kidney reabsorption and secretion functions were expressed in PT (Figures 3A and S5A), at comparable levels to PT cells in the postnatal kidney control (Figure S5B), with similar open chromatin accessibility (Figure S5C). The uptake of dextran[8] and albumin[10] demonstrated PT cell-mediated endocytotic activity in mKPAs (Figures S6A and S6B). Basally positioned organic cation/anion transporters (OCTs and OATs) mediate basal uptake of a broad spectrum of compounds, detoxifying the circulation in the mammalian kidney.[48] We observed cimetidine-dependent DAPI transport[10] specifically by the LRP2$^+$ PTs in the mKPAs (Figures 3B and S6C), indicating OCT function. The observed probenecid-dependent 6-carboxyfluorescein (6-CF) transport[49] (Figures 3C and S6D), as well as methotrexate[5] and penicillin[50] transport (Figures S6E and S6F), highlighted OAT function.

The kidney's major endocrine functions[51] were also recapitulated in the mKPAs under physiologically relevant experimental conditions: (1) in the presence of forskolin to activate cyclic AMP (cAMP) activity, renin was induced at both the mRNA and the protein levels[52] (Figures S6G and S6H); (2) in a vitamin D3 substrate 25(OH)D_3-dependent manner, parathyroid hormone (PTH) synergistically induced the expression of *Cyp24a1* and *S100g*, genes encoding critical enzymes that regulate vitamin D3 metabolism (Figure S6I); and (3) erythropoietin (EPO) was secreted when mKPAs were exposed to hypoxic conditions (4% O_2) (Figures S6J–S6L).

To facilitate mKPA vascularization and connection to circulation for further functional analysis, we next transplanted mKPAs to the mesentery of immunodeficient NOD.Cg-*Prkdc*^{scid}*Il2rg*^{tm1Wjl}/SzJ (NSG) mice (Figure 3D). mKPAs were assembled from *Six2*-tdT NPCs to allow lineage-tracing of NPC descendants and grafted at an early stage (day 3, equivalent to E11.5/E12.5 kidneys) to allow for improved growth and vascularization following experiments on early embryonic kidney transplantation.[53–60]

14–27 days after transplantation, large cystic structures were formed in the mKPAs that were largely negative for tdT, indicative of a UPC/CD origin (Figure 3E). Cyst fluid was collected and analyzed for urine components. Both creatinine and urea were enriched 57.3- and 20.2-fold, respectively, in the cyst fluid (11.47 ± 1.99 and 433.14 ± 10.75 mg/dL) when compared with serum (0.20 ± 0.06 and 21.43 ± 2.33 mg/dL, respectively; Figure 3F). Whole-mount immunostaining confirmed extensive nephron and CD development (Figure 3G). Importantly, tdT$^-$/PODXL$^+$ vasculature was identified, forming web-like structures covering the whole transplant and infiltrating into the glomeruli (Figures 3G and 3H). Consistent with initial macroscopic observation (Figure 3E), confocal images confirmed cyst-lining epithelial cells to be tdT$^-$/GATA3$^+$, consistent with CD originating from UPCs (Figure 3G). Transplanted mKPAs expressed major nephron and CD marker genes at levels comparable to or higher than a P0 mouse kidney, with dramatic elevation of endothelial cell marker genes *Pecam1* (*Cd31*) and *Cd146*, as expected (Figure S6M). Interestingly, many of the marker genes were further elevated in the mKPAs *in vivo* compared with *in vitro* counterparts, suggesting additional maturation of cell types *in vivo*. Intravital multiphoton microscopy following injection of lucifer yellow (LY) into the host circulatory system demonstrated dye entering the glomerulus through the afferent arteriole (AA), exiting through the efferent arteriole (EA), and glomerular perfusion (Figures 3I and 3J).

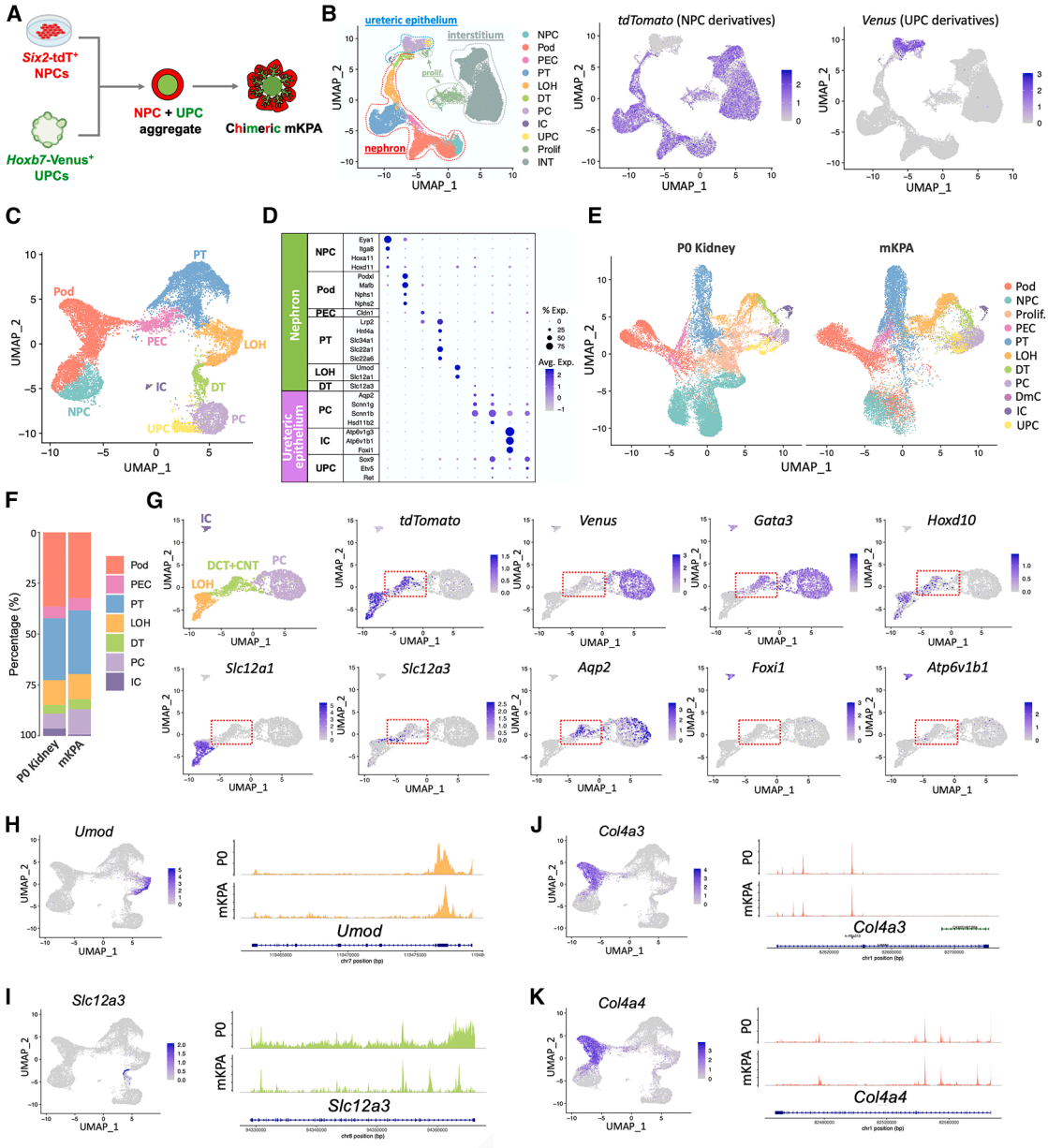

Figure 2. Single-cell multiome analyses of mKPAs

(A) Schematic of the generation of chimeric reporter mKPA for lineage tracing.

(B) UMAP (uniform manifold approximation and projection) visualization of cell types in day 24 mKPA and *tdTomato* and *Venus* gene expression. Pod, podocyte; PEC, parietal epithelial cell; PT, proximal tubule; LOH, loop of Henle; DT, distal tubule; PC, principal cell; IC, intercalated cell; Prolif., proliferative cell; INT, interstitium; DmC, deep medullary cell.

(C) UMAP visualization of NPC, UPC, and derivatives from snRNA-seq of mKPA.

(D) Dot plot of marker gene expression from snRNA-seq arranged by group and cell type.

(E) UMAPs showing the integration of snRNA-seq data (nephron and ureteric epithelium) of day 24 mKPA with P0 kidney.

(F) Bar graph showing the proportions of nephron and CD cell types identified from (E).

(G) UMAP projection of the expression of marker genes in subclustered LOH, DT, PC, and IC populations of the day 24 mKPA.

(H–K) UMAP of snRNA-seq (left) and genome browser views of snATAC-seq open chromatin regions (right) of selected genes from mKPA as compared with P0 kidney.

Assembly of spatially patterned hKPAs from iNPCs and iUPCs

Starting from our previously described expandable hPSC-induced NPCs (iNPCs) and UPCs (iUPCs),[11,14] and based on a culture system slightly modified from the v2 medium (designated as "v3 medium") (Figure S7A; Methods S2 and S3; STAR Methods), we developed spatially patterned hKPAs. A *PAX2*-mCherry reporter[14] in iUPCs and a *SIX2*-GFP reporter[11]

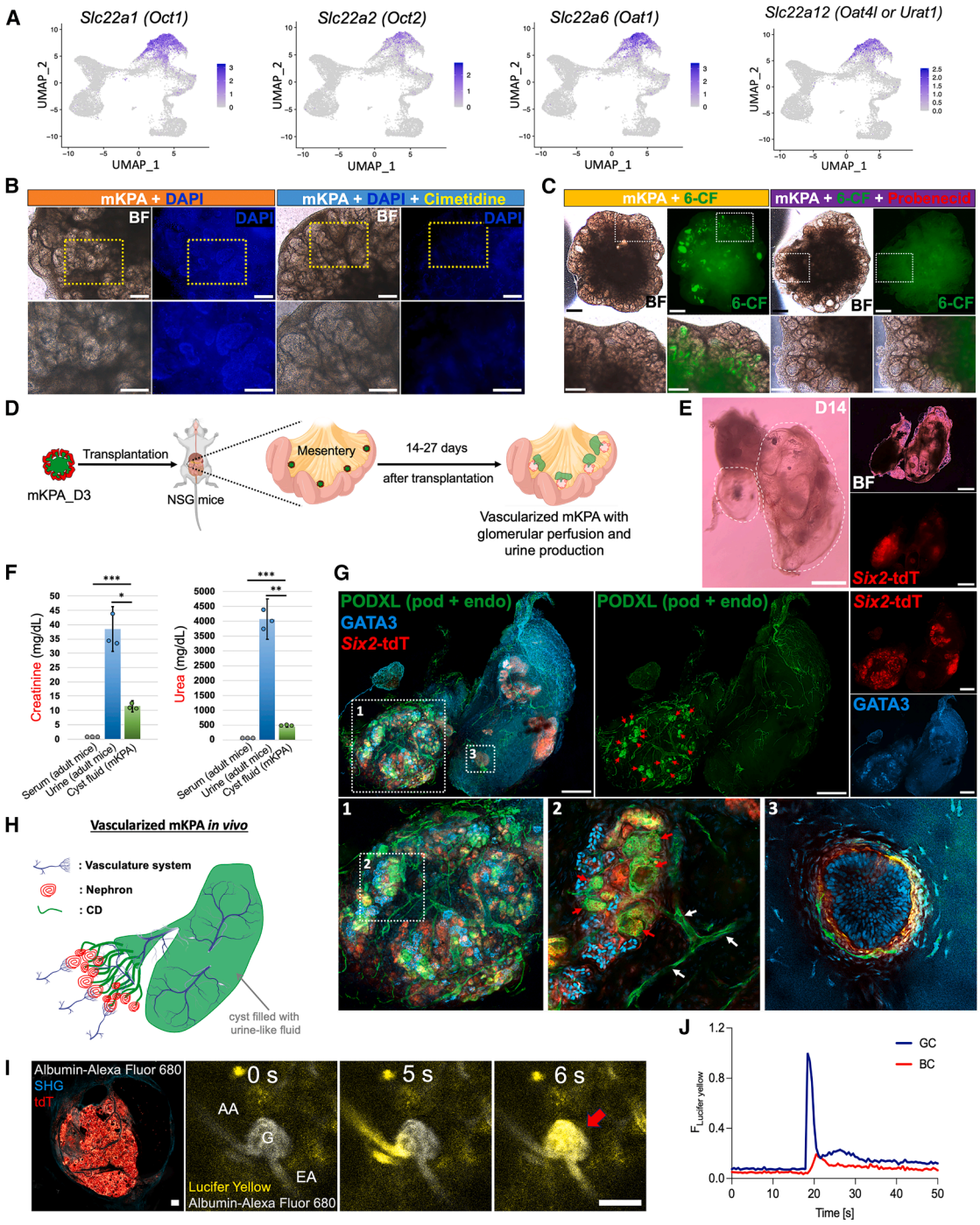

Figure 3. Functional maturation of mKPAs *in vitro* and *in vivo*

(A) UMAP projection of gene expression.

(B and C) Live images of day 20 mKPAs with treatments as indicated. Enlarged pictures of the boxed areas from the upper panels are shown in the lower panels. Scale bars, 500 μm (upper panels of C), 100 μm (upper panels of B and lower panels of C), and 50 μm (lower panels of B).

(D) Experimental protocol for day 3 mKPA transplantation.

(E) BF and *Six2*-tdT fluorescence images of an mKPA dissected 14 days post transplantation. Scale bar, 500 μm.

(F) Quantification of urea and creatinine levels in the serum and urine of adult mice and in the cyst fluid of mKPAs.

(G) Whole-mount immunofluorescence analysis of an mKPA dissected 14 days post transplantation. Enlarged pictures of the numbered boxed areas are shown in the lower panels. Red arrows indicate the mKPA's round glomeruli. White arrows highlight some host blood vessels infiltrating into the glomeruli. Endo, endothelial cells. Scale bars, 500 μm.

(H) Schematic of the structure of a vascularized mKPA transplant.

(legend continued on next page)

in iNPCs were used to track iUPC-derived UB and CD and undifferentiated NPCs, respectively.

Between days 5 and 9, a clear mesenchymal-to-epithelial transition (MET) was observed in the iNPCs, forming an array of epithelialized RV structures adjacent to the central UB (Figures 4A–4C, S7B, and S7C; Video S4). These RV structures developed a clear lumen and transitioned gradually from a homogeneous WT1$^+$/JAG1$^+$/CDH1$^+$ early RV to a polarized RV with a CDH1$^+$/JAG1$^-$/WT1$^-$ distal pole, a JAG1$^+$/CDH1$^-$/WT1$^-$ intermediate region, and a WT1$^+$/JAG1$^-$/CDH1$^-$ proximal pole, before the distal pole was fused to the central iUPC-derived UB (Figure 4C, follow the arrows for gradual transition of RV), resembling the developing nephron anlagen *in vivo*.[61] Interestingly, iNPCs far from the central UB died, as revealed by TUNEL (terminal deoxynucleotidyl transferase dUTP nick end labeling) assay (Figures S7D and S7E), reflecting NPC's default apoptosis fate in the absence of the UB-derived signals.[62,63] These RV structures underwent a progressive morphogenesis, forming elongated nephron tubules orientated to the central UB/CD (Figures 4D–4F; Video S4). Immunostaining identified spatially organized nephrons with round NPHS1$^+$ glomerulus-like structures at the periphery, connected to HNF4A$^+$ PT, POU3F3$^+$/CDH1$^+$/SLC12A1$^+$ LOH, followed by POU3F3$^+$/CDH1$^+$/SLC12A1$^-$ DN segments (Figures 4F and S7F). Importantly, multiple segmented nephrons were identified in each hKPA, with DN connected to the central CD (Figures 4E, 4F, and S7F–S7H), forming a continuous tubule structure with the iUPC-derived *PAX2*-mCherry$^+$/GATA3$^+$/CDH1$^+$ CD and the iNPC-derived *PAX2*-mCherry$^-$/GATA3$^+$/CDH1$^+$ DN (Figure S7H). hKPAs were healthy after 30 days of *in vitro* development, exhibiting minimal cell death (Figures S7I and S7J). Importantly, the hKPA protocol is highly reproducible, as demonstrated in two additional human induced PSC (iPSC) lines, the wild-type WTC-11 line (Mendeley Data Figure S4; Methods S4) and the Alport syndrome patient line CIRC-2 (Mendeley Data Figure S5; Methods S4), both exhibiting polarized RVs that progressed into segmented nephrons connected to the central collecting system.

We observed that TTNPB, an agonist of the retinoic acid (RA) signaling pathway, is essential for polarized RV formation and spatial patterning of hKPAs in multiple hPSC lines (Figures S8A and S8B). In the absence of TTNPB, RVs either failed to form or were dramatically reduced (Figures S8C–S8F), resulting in either completely failed hKPA development (no nephron induction) or disorganized nephron induction without connection to the CD (Figures S8G–S8I). To understand the mechanism, we used snRNA-seq to profile the hKPAs cultured with or without TTNPB for 6 days ("+TT" or "−TT," respectively). In both samples, NPCs, UPCs, SSB-stage early Pod (SSB-Pod), early renal tubule cells (SSB-distal), intermediate distal progenitor cells (DP), and interstitial cells were identified, recapitulating early nephrogenesis *in vivo*[47,64] (Figure 4G; Mendeley Data Figures S6A and S6B). Analysis of gene expression confirmed RA signaling activation in the +TT samples (Mendeley Data Figures S6C–S6E). In the absence of TTNPB, NPC population was increased, and DP population was decreased (Figure 4H), consistent with reduced RV induction observed (Figures S8C–S8F), suggesting inhibited nephrogenesis. Differentially expressed genes (DEGs) were identified for each cell cluster (Table S2). Interestingly, *WNT4*, a gene with a well-established role as a molecular switch controlling NPC differentiation to RV,[65–68] was dramatically decreased in the nephron cell types (NPC, DP, and SSB-distal) in the absence of TTNPB (Figure 4I). These data suggest that activation of RA signaling enables NPCs to form polarized RVs, likely through the induction of *WNT4*. In supporting this, analysis of the human fetal kidney snRNA-seq dataset[47] confirmed *WNT4* expression in the differentiating NPCs and RV cell types, as well as the activation of RA signaling in the human fetal kidney (Figures 4J–4M; Mendeley Data Figures S6F and S6G).

Single-nuclear multiome analysis on day 25 identified major human nephron and CD cell types. Undifferentiated NPCs were still maintained over this period, but UPCs were absent. In addition, interstitial cells, endothelial cells, and a small population of neural-like cells were identified (Figure S9; Table S2). hKPAs have features in common with the 17-week human fetal kidneys[47] (Figures 4N, 4O, S10A–S10G, and S11A), although ICs were not detected. Consistent with the observed tubular connection between DN and CD by bright-field and confocal imaging, snRNA-seq clearly identified a *GATA3*$^+$/*CALB1*$^+$/*AQP2*$^+$/*SCNN1G*$^+$/*TMEM52B*$^+$ CNT population within the DN, in close proximity to the *GATA3*$^+$/*CALB1*$^+$/*AQP2*$^+$/*SCNN1G*$^+$/*TMEM52B*$^-$ PC population in the UMAP plot (Figure S10H). Using marker genes identified in mouse kidneys,[46] human interstitium can be subclustered into cortical, medullary, CD-associated, and ureteric stromal cells (Figures S11B and S11C). Comparisons of snRNA-seq datasets from hKPAs and conventional kidney organoids[2,4,19,69] confirmed the presence of CD cell types (PC and deep medullary cell [DmC]) only in the hKPAs and higher similarity of hKPA's kidney cell types to 17-week human fetal kidney as compared with conventional kidney organoids (Figure S11D). Consistent with the gene expression, the hKPAs exhibit tubular reabsorption and secretion functions *in vitro* (Figures 4P, 4Q, S7K, and S7L).

Generation of vascularized and functional hKPAs upon transplantation *in vivo*

Although some tubular functions can be determined in the hKPAs grown *in vitro*, the lack of vasculature prevents further functional analysis. We thus transplanted the RV-stage hKPAs

(I) Tile-scan overview of tdT-labeled mKPA transplant illuminated by second harmonic generation (SHG, cyan) (left). Representative time-lapse images of a single glomerulus (G) in the mKPA transplant before (0 s) and after (5 and 6 s time points) the intravenous (i.v.) injection of the fluid marker lucifer yellow (LY, yellow) into the host mouse (right). AA, afferent arteriole; EA, efferent arteriole. The red arrow indicates glomerular filtration of LY from glomerular capillaries (GCs) into the surrounding Bowman's space. Scale bar, 100 μm.

(J) Recording of LY fluorescence intensity (F) changes over time during i.v. LY injection in GCs (blue line) and in the Bowman's space (red).

Data are presented as mean ± SD. Each column represents counts from three biological replicates (n = 3). The significance was determined by two-tailed unpaired Student's t tests; ns, not significant; *p < 0.05, **p < 0.01, ***p < 0.001.

See also Figures S5 and S6.

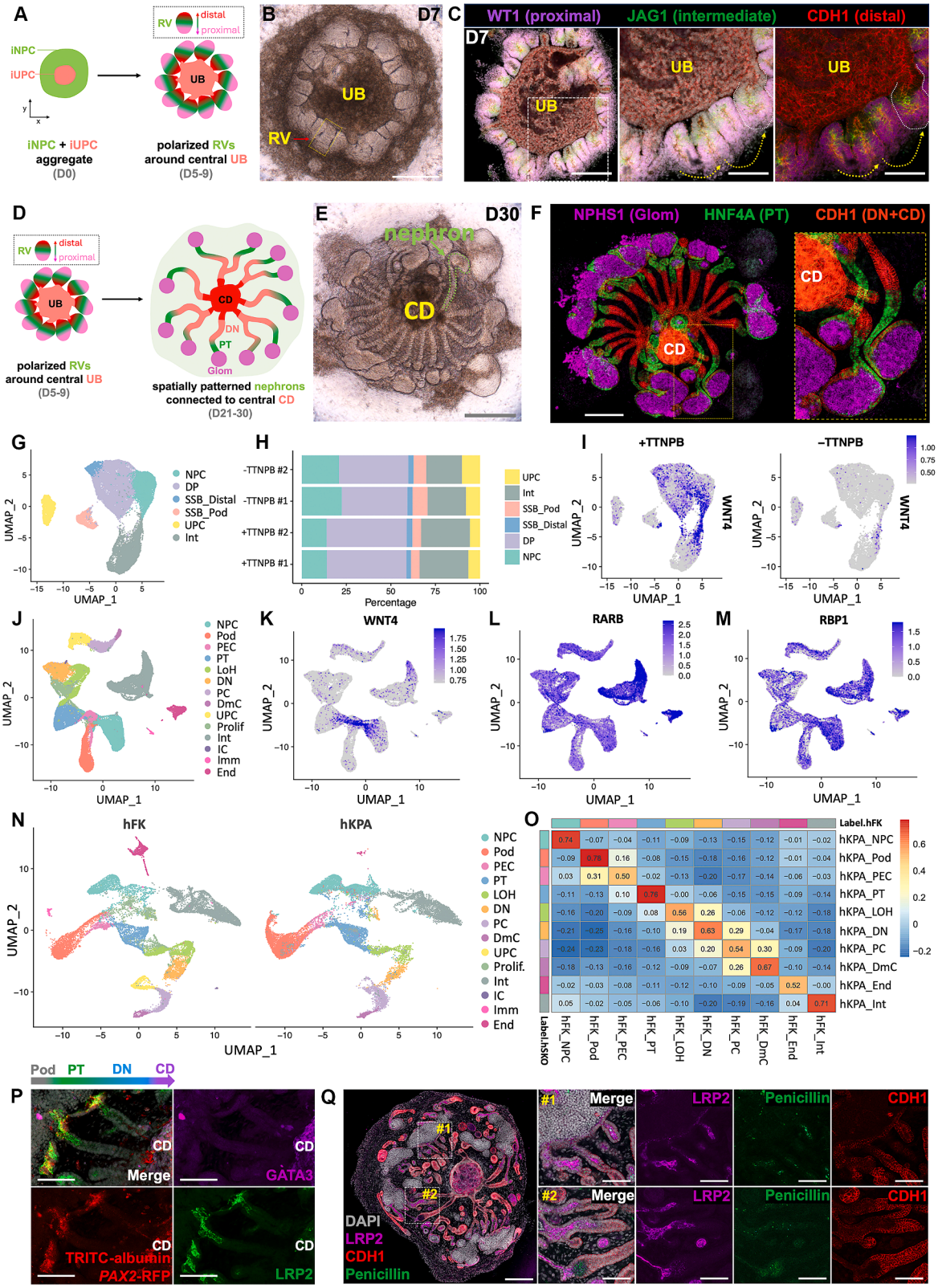

Figure 4. Assembly of spatially patterned hKPAs from iNPCs and iUPCs

(A) Schematic of polarized RV formation in early hKPA.

(B) BF image of a representative day 7 hKPA. The boxed area highlights one RV. Scale bar, 200 μm.

(legend continued on next page)

into the renal capsule of NSG mice (Figure 5A). 1 month after transplantation, hKPAs grew significantly in size (Figure S12A) and showed extensive vascularization (Figures S12B and S12C; Video S5). Glomeruli showed evident Bowman's space, with the presence of DESMIN$^+$/PDGFRB$^+$ MCs adjacent to NPHS1$^+$ Pod (Figures 5B and S12D). Interestingly, based on immunostaining with species-specific CD31 antibodies, we observed that a significant portion of the hKPA's glomeruli (36.4%) had glomerular capillaries exclusively from the human species, with the majority of the glomeruli (54.5%) bearing chimeric capillaries from both mouse and human species (Figures 5C, 5D, and S12E), revealing the unexpected plasticity of iNPC and iUPC co-culture to generate human endothelial cells *in vivo*. Outside the glomeruli, CD31$^+$ cells were frequently found to wrap around the renal tubules, suggesting the formation of peritubular capillaries (Figure S12F). Elongated renal tubules formed *in vivo*, with their distal ends connected to the central CD (Figures 5E and S12G). PDGFRB$^+$ interstitial cells were formed surrounding the hKPA's nephrons and CD, exclusively from human species (Figures 5F, S12H, and S12I).

Profiling of hKPAs with snRNA-seq confirmed the diversity of major human nephron and CD cell types in hKPAs, though ICs were not detected (Figures 5G and S13A–S13E). It also verified the formation of human vasculature and stroma. Mouse vasculature and macrophages were identified, as well as a small number of mouse stroma, PT, and PC. We compared hKPA's transcriptome with that of human fetal[47] and adult[22] kidneys. Statistical gene set score analysis with the top 500 DEGs between human fetal and adult kidneys (Table S2) unbiasedly indicated hKPAs express this set of maturity-related signature genes higher than human fetal kidneys, although still lower than adult kidneys (Figures 5H and 5I). Further analysis of the DEGs that are expressed higher in both hKPAs and adult kidneys compared with fetal kidneys highlighted Pod expression of *COL4A3*, *COL4A4*, and *COL4A5*, key collagens of mature Pod,[69] which are mutated in patients with Alport's syndrome,[70,71] as well as *PLA2R1*, a human Pod-specific gene associated with membranous nephropathy[72] (Figure 5J). In the PT and LOH, a significant increase in a large number of genes involved in oxidative phosphorylation was observed, consistent with the increased mitochondria demand required in the mature renal tubules for active transport activities[73] (Figures 5K and 5L). Importantly, a large number of genes that mediate critical kidney functions that were not expressed in current kidney organoids,[16–19] such as *SLC22A2* (*OCT2*), *SLC22A6* (*OAT1*), and *SLC5A2* (*SGLT2*), were expressed in the hKPAs grown *in vivo* (Figure S13F). Head-to-head comparison with a human kidney organoid transplanted *in vivo*[17] clearly indicated the presence of CD cell types (PC and DmC) only in the hKPAs, with significantly increased maturity (Mendeley Data Figure S7).

Intravital multiphoton microscopy recorded real-time glomerular perfusion (Figures 5M and 5N) and the uptake of albumin to the hKPA's PT expressing endogenous *PAX2*-mCherry reporter, suggesting tubular reabsorption (Figure 5O). When the tubules were dissected for patch-clamp analysis, ion channel activities (K^+) were recorded on the basolateral side of the tubule membrane (Figure 5P). Small numbers of RENIN$^+$ cells were identified near the hKPA's glomeruli around human CD31$^+$ vasculature (Figures 5Q and S12J), suggesting endocrine function. In rare cases, we identified slight swelling of the GATA3$^+$/CDH1$^+$ DN/CD compartment, but the small size prevented us from collecting any fluid for urine component analysis (Figure S12K). hKPAs grown *in vivo* were overall healthy with limited cell death (Figures S12L and S12M).

High-fidelity *in vivo* modeling of human ADKPD

The hKPA grown *in vivo* can closely recapitulate the complexity of human kidney anatomy and function. To provide a proof-of-concept for its clinical application, we used it to model autosomal dominant polycystic kidney disease (ADPKD), the most prevalent inherited kidney disease, mainly caused by loss of function of *PKD1* or *PKD2* genes.[74] We assembled *PKD2*$^{-/-}$ hKPAs from our previously described *PKD2*$^{-/-}$ iNPC line[11] and the *WNT11*-GFP/*PAX2*-mCherry iUPC line.[14] Similar to wild-type hKPAs, *PKD2*$^{-/-}$ hKPAs developed the signature polarized RVs around the central UB 5 days after assembly (Mendeley Data Figures S8A–S8C). 2 months after these RV-stage *PKD2*$^{-/-}$ hKPAs were transplanted into NSG mice, the transplants grew to the size of the host mouse kidney with evidence of numerous cystic structures. By strong contrast, no cysts were observed from the wild-type hKPA transplants (Figures 6A and 6B; Mendeley Data Figures S8D and S8E). Quantification of cystic (*PKD2*$^{-/-}$) or tubular (wild-type) lumen sizes confirmed dramatic cyst development from the *PKD2*$^{-/-}$ hKPAs (Figures 6C and 6D). In strong contrast to conventional *in vitro* ADPKD kidney organoid models[75,76] in which primary cilia had reversed cell membrane localization, primary cilia in the *in vivo*-grown *PKD2*$^{-/-}$ hKPAs exclusively point to the cyst lumen as found in ADPKD patients[74,77,78] (Figure 6C). Nearly all the cells of the cystic epithelium of *PKD2*$^{-/-}$ hKPAs stained positive for

(C) Whole-mount immunofluorescence analysis of a day 7 hKPA. Enlarged pictures of the boxed area are shown in the middle and right panels. Scale bar, 200 μm.
(D) Schematic of hKPA transition from RV stage to later stage forming connected nephrons and CD.
(E) BF image of a day 30 hKPA. Yellow dotted line outlines a single nephron. Scale bar, 200 μm.
(F) Whole-mount immunofluorescence analysis of a day 30 hKPA. Enlarged picture of the boxed area is shown in the right panel. Scale bars, 200 μm.
(G) UMAP visualization of cell clusters identified by snRNA-seq in day 6 hKPAs cultured with or without TTNPB.
(H) Bar graph showing the proportions of cell populations identified from (G).
(I) UMAP projection of the expression of *WNT4* in day 6 hKPAs cultured with or without TTNPB.
(J) UMAP visualization of the cell clusters identified in 17-week human fetal kidney (hFK) by snRNA-seq. Imm, immune cell; End, endothelium cell.
(K–M) UMAP projection of gene expression in 17-week hFK.
(N) UMAP projection of cell populations identified from integrated day 25 hKPA and 17-week hFK datasets.
(O) Pearson correlation coefficient (PCC) matrix heatmap for common cell types identified between hFK and hKPA.
(P and Q) Whole-mount immunofluorescence analysis of day 21 hKPAs treated with TRITC-albumin (P) or BOCILLIN FL penicillin (Q). Enlarged pictures of the boxed areas (#1 and #2) are shown on the right panels. Scale bars, 100 μm (P) and 200 μm (Q).
See also Figures S7–S11.

CellPress

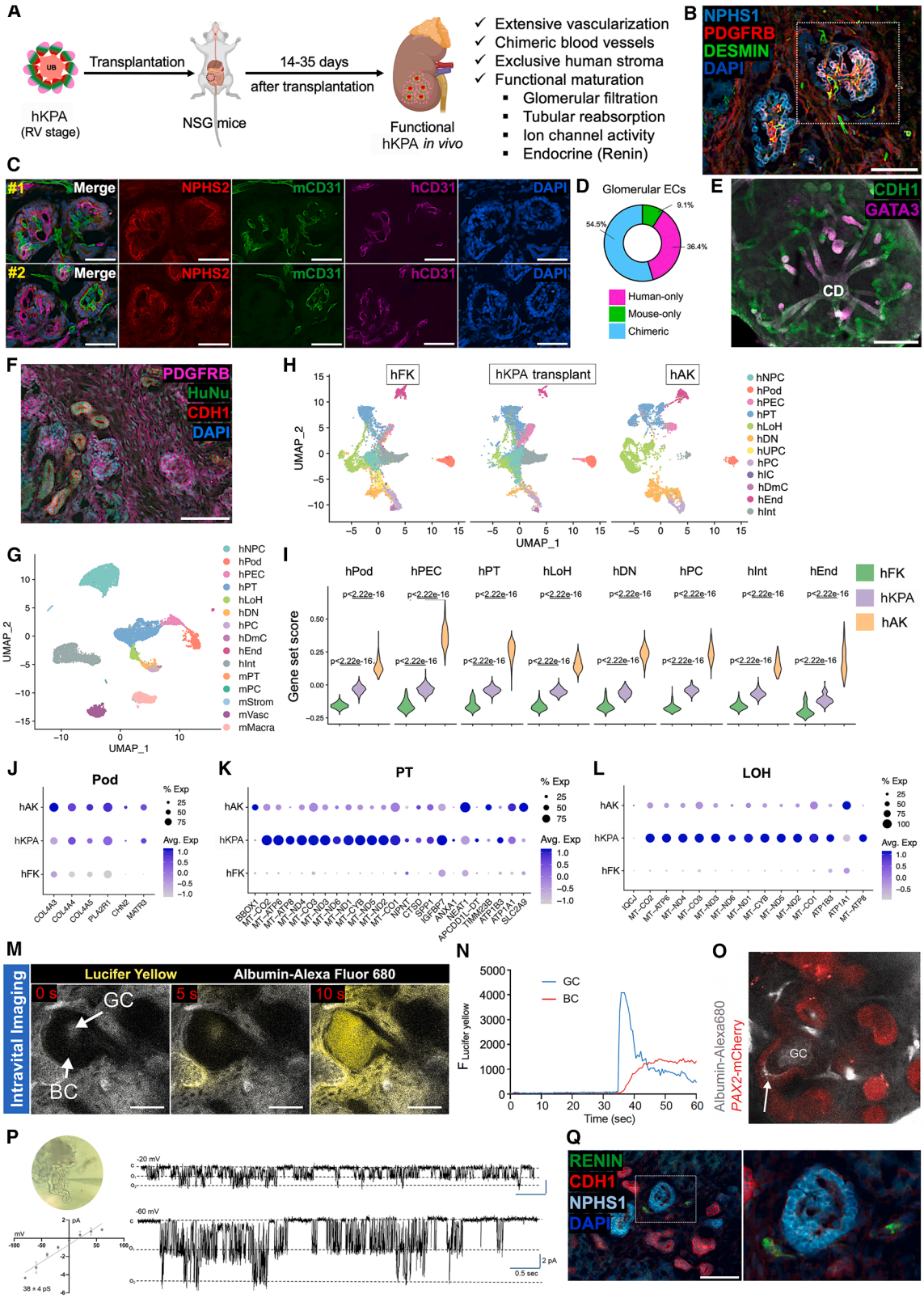

Figure 5. Generation of functional hKPA upon transplantation *in vivo*

(A) Schematic of hKPA transplantation and summary of features of hKPAs grown *in vivo*.

(B) Immunofluorescence image of a cryosection of an hKPA transplant. Enlarged pictures of the white boxed area are shown in Figure S12D. Scale bar, 50 μm.

(legend continued on next page)

the cell proliferation marker PCNA (Figures 6E and 6F), reflecting active proliferation. Using ZO-1 staining, different phases of loss of epithelial cell polarity were captured, exhibiting sequential ZO-1 expression on the apical side (phase I, pre-cystic), on the basolateral side (phase II, cyst in development), or complete loss of ZO-1 expression (phase III, latest stage) (Figures 6G and 6H; Mendeley Data Figure S8F). In ADPKD, changes in cystic epithelium trigger fibrosis in the surrounding stromal cells, a key mechanism leading to further disease progression,[79] which cannot be recapitulated *in vitro*. We observed the formation of a condensed thick layer of PDGFRB$^+$/MEIS1$^+$/COL1A1$^+$/FN1$^+$/ACTA2$^+$/DESMIN$^+$ human myofibroblast cells surrounding the cysts of the *PKD2*$^{-/-}$ hKPAs, which was absent from the wild-type hKPAs (Figures 6I–6R and 6W; Mendeley Data Figures S8G–S8K). CD45$^+$ and F4/80$^+$ immune cells were found to cluster around the cyst epithelium in *PKD2*$^{-/-}$ hKPAs, suggesting macrophage infiltration, another hallmark of ADPKD[80–84] that cannot be recapitulated *in vitro* (Figures 6S–6V; Mendeley Data Figures S8L and S8M). Interestingly, collection of cyst fluid from the large cysts of *PKD2*$^{-/-}$ hKPAs for urine component analysis indicated dramatic elevation of creatinine and urea (Mendeley Data Figures S8N and S8O).

snRNA-seq analysis of the *in vivo* ADPKD model sheds light on disease mechanisms

We next performed snRNA-seq to further characterize the *in vivo* ADPKD model and compared the findings with that from ADPKD patient samples.[85] Similar to 1-month wild-type hKPA transplants (Figure 5G), 2-month *PKD2*$^{-/-}$ and wild-type hKPA transplants also showed the presence of NPCs, major human nephrons (Pod, PEC, PT, LOH, and DN), CD (PC and DmC), interstitial and endothelial cells, as well as mouse endothelial cells, macrophages, and a small number of mouse stroma, PT, and PC (Figures 7A and S14A). No major differences in cell population abundances were observed between *PKD2*$^{-/-}$ and wild-type hKPA transplants (Figure S14B). DEG analysis highlighted human PT (hPT) and human interstitial cells (hInt) as the two cell types that have the highest DEG numbers, consistent with the critical roles hPT and hInt play in ADPKD (Figure S14C). Consistent with the notion that wild-type iUPCs were used to assemble *PKD2*$^{-/-}$ hKPAs, human PC (hPC) cluster has one of the lowest numbers of DEGs. Thus, we focused on hPT and hInt for further analysis. Gene Ontology (GO) analysis highlighted the activation of cAMP, phosphatidylinositol 3-kinase (PI3K)/AKT, mTOR, and Wnt signaling (Figures 7B and 7D), and a dramatic decrease of oxidative phosphorylation (Figures 7C and 7E) in the *PKD2*$^{-/-}$ hPT as compared with the wild type, recapitulating changes of major pathogenic pathways and metabolic reprogramming that are well-established hallmarks in the cystic epithelium of ADPKD.[74] Extracellular matrix organization genes were enriched in the *PKD2*$^{-/-}$ hInt (Figures 7F, 7G, and S14D), consistent with the formation of a collagen/fibronectin-enriched myofibroblast cell layer around the cysts as revealed by immunostaining (Figures 6I–6R). CellChat[86] revealed an overall increased number and strength of signaling interactions in the *PKD2*$^{-/-}$ hKPAs (Figure S14E). Strong transforming growth factor β (TGF-β) signaling sending from hPT to hInt, as well as its autocrine activation within hPT, was identified in the *PKD2*$^{-/-}$ but not in the wild-type hKPAs (Figure 7H). Interestingly, a similar crosstalk to that predicted here has been reported in ADPKD patient samples[85] (Figure S14F). Importantly, hKPA datasets and ADPKD patient datasets share several predicted signaling interactions implicated in kidney disease progression, including SEMA3 (semaphorin 3),[87–90] EPHB (erythropoietin-producing human hepatocellular receptor B),[91–93] and non-canonical Wnt signaling pathways[94–96] (Figures 7I–7K and S14G–S14I), which warrant future investigation (see also Table S2 for a full list of top candidate pathways identified).

Macrophages play critical roles in ADPKD progression.[97] To determine whether this is recapitulated in the *in vivo* ADPKD model, we first used biomaRt[98,99] to convert mouse gene symbols to their human orthologs and then merged the humanized mouse matrix and the human matrix using Seurat[100] for CellChat[86] analysis (Figure 7L; Mendeley Data Figures S9A and S9B). Signaling pathways highlighted in the *PKD2*$^{-/-}$ hKPA transplants include COLLAGEN, APP (amyloid beta precursor protein), CADM (cell adhesion molecule), SIRP (signal regulatory protein), SEMA3, SEMA6, CD45, and NOTCH (Figures 7M and 7N; Mendeley Data Figures S9C and S9D). Notably,

(C) Immunofluorescence image of a cryosection of an hKPA transplant. #1 and #2 are enlarged pictures of selected areas from Figure S12E. Scale bar, 50 μm.
(D) Quantification of glomerulus endothelial cell (EC) compositions found in hKPA transplants.
(E) Whole-mount immunofluorescence image of an hKPA transplant. See also Figure S12H for split channel images. Scale bar, 200 μm.
(F) Immunofluorescence image of a cryosection of an hKPA transplant. See also Figure S12I for split channel images. Scale bar, 50 μm.
(G) UMAP visualization of cell clusters identified from day 32 hKPA transplants by snRNA-seq. mMac, mouse macrophage.
(H) UMAPs showing the integration of snRNA-seq data of day 32 hKPA transplants, 17-week hFK, and human adult kidney (hAK).
(I) Violin plot showing the gene set scores of cell-type-specific maturation signatures in corresponding cell types from hFK, hAK, and hKPA transplant.
(J–L) Dot plots of marker gene expression in Pod (J), PT (K), and LOH (L) populations in day 32 hKPA transplant, hFK, and hAK.
(M) Representative time-lapse intravital multiphoton images of a single glomerulus in the hKPA transplant before (0 s) and after (5 and 10 s time points) the i.v. injection of the fluid marker LY (yellow) into the host mouse. GC, glomerular capillary; BC, Bowman's capsule. Scale bars, 100 μm.
(N) Recording of LY fluorescence intensity (F) changes over time during i.v. LY injection in GCs (blue line) and in the Bowman's space (red).
(O) Representative intravital multiphoton image of a *PAX2*-RFP hKPA transplant after i.v. injection of albumin-Alexa 680 (white) into the host mouse. White arrow indicates the accumulation of albumin-Alexa 680 in the renal tubules. Scale bar, 100 μm.
(P) Representative image showing the patch-clamp setup (top left). Corresponding single-channel potassium-like currents were recorded from the same patch at varying pipette potentials, demonstrating inwardly rectifying behavior (right). The average single-channel conductance was 38 ± 4 pS (n = 5). Downward deflections represent inward currents. The solid line indicates the non-conducting closed state (c), while dashed lines denote open states (o). The current-voltage (I-V) relationship showing the average unitary current amplitude for the recorded potassium channels is shown on the lower left panel. Data are presented as mean ± SEM.
(Q) Immunofluorescence image of a cryosection of an hKPA transplant. Enlarged picture of the white boxed area is shown in the right panel. Scale bar, 50 μm. See also Figures S12 and S13.

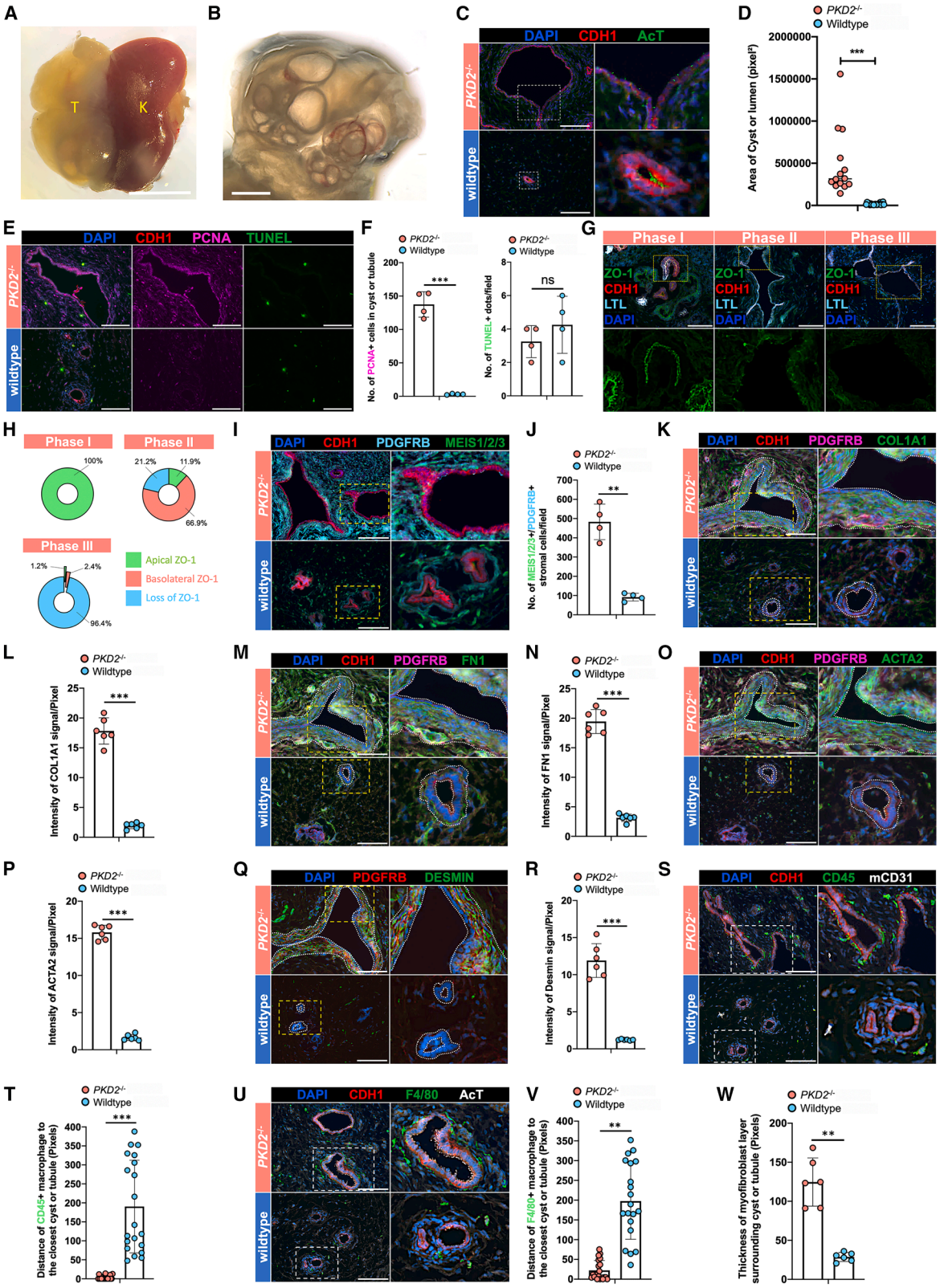

Figure 6. High-fidelity *in vivo* modeling of human ADPKD with *PKD2*$^{-/-}$ hKPA

(A) Image of a mouse kidney harboring *PKD2*$^{-/-}$ hKPA transplants 66 days post transplantation. Scale bar, 5 mm.

(B) Image of dissected *PKD2*$^{-/-}$ hKPA transplants shown in (A). Scale bar, 2 mm.

(legend continued on next page)

macrophages from *PKD2*$^{-/-}$ hKPA transplants had enriched NOTCH signaling, which is associated with a pro-inflammatory macrophage phenotype and ADPKD progression[101–103] (Figure 7O; Mendeley Data Figure S9E). Macrophages from *PKD2*$^{-/-}$ hKPA transplants also had higher expression of pro-inflammatory and pro-fibrotic genes, including *Adamts12*, *Thbs2, Ikbip*, and *Col1a1*, compared with macrophages from wild-type hKPA transplants (Figure 7P). Collectively, these data strongly support the fidelity of the *in vivo* hKPA-based ADPKD model and shed light on novel disease mechanisms (Figure 7Q).

DISCUSSION

Successful development of mKPAs and hKPAs relies on (1) the ability to generate high-quality and high-purity kidney progenitor cells *in vitro* that resemble their *in vivo* counterparts[11,14] and (2) the development of optimal kidney culture systems that support reciprocal mouse (v2 medium) and human (v3 medium) kidney progenitor interactions leading to improved spatial patterning, maturity, and functionality. Compared with the transient hPSC-derived iNPCs,[2,4] the expandable human iNPCs used in this study have been shown to be programmed to a state that is closer to the native human NPCs *in vivo*,[11] and the expandable human iUPCs used are a near-pure progenitor population,[14] unlike other human UB organoids that develop a mixture of both UB tip (progenitor cells) and UB trunk (differentiated cells) structures.[13,15,33,34]

Reciprocal interactions between pure iNPCs and iUPCs induced the formation of polarized RVs around the central UB, a distinctive feature that is not found in any other human kidney organoids.[1–15,37–41] Polarized RVs further progress into segmented nephron tubules that are fused to the central CD, also unique in the hKPA model. The exhibition of key kidney functions—including glomerular perfusion, tubular reabsorption and secretion, and endocrine activity—makes hKPAs well-suited for studies of kidney physiology and pathophysiology, a level of functionality not achieved in current kidney organoid models.[1–15,37–41]

This study reveals multiple cases of kidney progenitor plasticity that warrant future investigations. In the mKPAs, a clear NPC-to-IPC transdifferentiation was observed, and in the hKPAs, the iNPC-iUPC co-culture appears to generate human glomerular-like capillaries and diverse populations expressing markers associated with human stroma *in vivo*. Whether NPC-to-IPC transdifferentiation is also present in hKPAs remains to be determined. Human glomerular capillaries are well developed *in vivo* but not *in vitro*, suggesting context-dependent progenitor plasticity.

Transplantation of *PKD2*$^{-/-}$ hKPAs *in vivo* recapitulated key molecular and cellular hallmarks of ADPKD, as well as the complex crosstalk among cyst epithelium, stroma, and macrophages in the microenvironment, which are not recapitulated in current ADPKD organoid models.[3,8,75,104–106] We have identified many potential early ADPKD-related pathogenic pathways and cell-cell crosstalk (Table S2), offering unique resources to further examine the mechanisms of early ADPKD development and to identify novel therapeutic targets. High-fidelity ADPKD modeling sets an example for the broad clinical application of the hKPA platform in disease modeling and drug discovery for kidney diseases.

Like embryonic kidneys,[53–60] transplantation of early-stage mKPAs or hKPAs *in vivo* resulted in the continued growth, differentiation, vascularization, and functional maturation of the transplants. These observations offer a strong foundation for further engineering of functional kidneys for transplantation.

Limitations of the study

Due to the unavailability of snRNA-seq datasets of human kidneys at later gestational stages, hKPAs grown *in vivo* were compared with 17-week human fetal kidneys (the latest fetal kidney dataset available) and adult human kidneys as the references, which suggested hKPAs were more mature than 17-week human kidneys. It remains to be determined whether hKPAs reached the maturity of neonatal human kidneys as the mKPAs. Unlike the mKPAs, sustained nephrogenic niche and branching morphogenesis in the hKPAs are still not achieved, representing important future directions. IC is absent from the hKPAs, consistent with its absence from all existing human CD organoids,[3,12,14,15] unless the IC-specific transcription factor FOXI1 was ectopically overexpressed.[15] These results suggest likely species differences in IC development,[47,61,107,108] or specific physiological cues are required to specify human IC. Limited by the availability of the *PKD2*$^{-/-}$ iUPC line, we were only able to provide a proof-of-concept in this study with a chimeric ADPKD hKPA model grown *in vivo* in which the nephrons and the stroma were *PKD2*$^{-/-}$, but the CDs were wild type. Future effort is warranted to generate a complete *PKD2*$^{-/-}$ hKPA model to recapitulate cystogenesis from all the kidney segments, including the CD.

RESOURCE AVAILABILITY

Lead contact

Further information and requests for resources and reagents should be directed to and will be fulfilled by the lead contact, Zhongwei Li (zhongwei.li@med.usc.edu).

(C) Immunofluorescence analysis of cryosections of wild-type and *PKD2*$^{-/-}$ hKPA transplants. Enlarged pictures of the white boxed areas are shown in the right panels. Scale bar, 50 μm.
(D) Quantification of the cyst (*PKD2*$^{-/-}$) or tubule (wild-type) lumen area based on (C).
(E and F) Immunofluorescence analysis (E) and quantification (F) of wild-type and *PKD2*$^{-/-}$ hKPA transplants. Scale bar, 50 μm.
(G) Immunofluorescence analysis of cryosections of wild-type and *PKD2*$^{-/-}$ hKPA transplants. Enlarged pictures of the yellow boxed areas are shown in the lower panels. Scale bar, 50 μm.
(H) Quantification of percentages of three stages of epithelial cell polarity.
(I–V) Immunofluorescence analysis (I, K, M, O, Q, S, and U) and quantification (J, L, N, P, R, T, and V) of cryosections of wild-type and *PKD2*$^{-/-}$ hKPA transplants. Enlarged pictures of the yellow boxed areas are shown in the right panels. Scale bar, 50 μm.
(W) Quantification of the thicknesses of myofibroblast layers surrounding *PKD2*$^{-/-}$ hKPA transplant cysts or wild-type hKPA transplant tubules based on images shown in (I), (K), (M), (O), and (Q).
Data are presented as mean ± SD. Each column represents counts from multiple biological replicates ($n > 3$). The significance was determined by two-tailed unpaired Student's t tests; ns, not significant; *$p < 0.05$, **$p < 0.01$, ***$p < 0.001$.

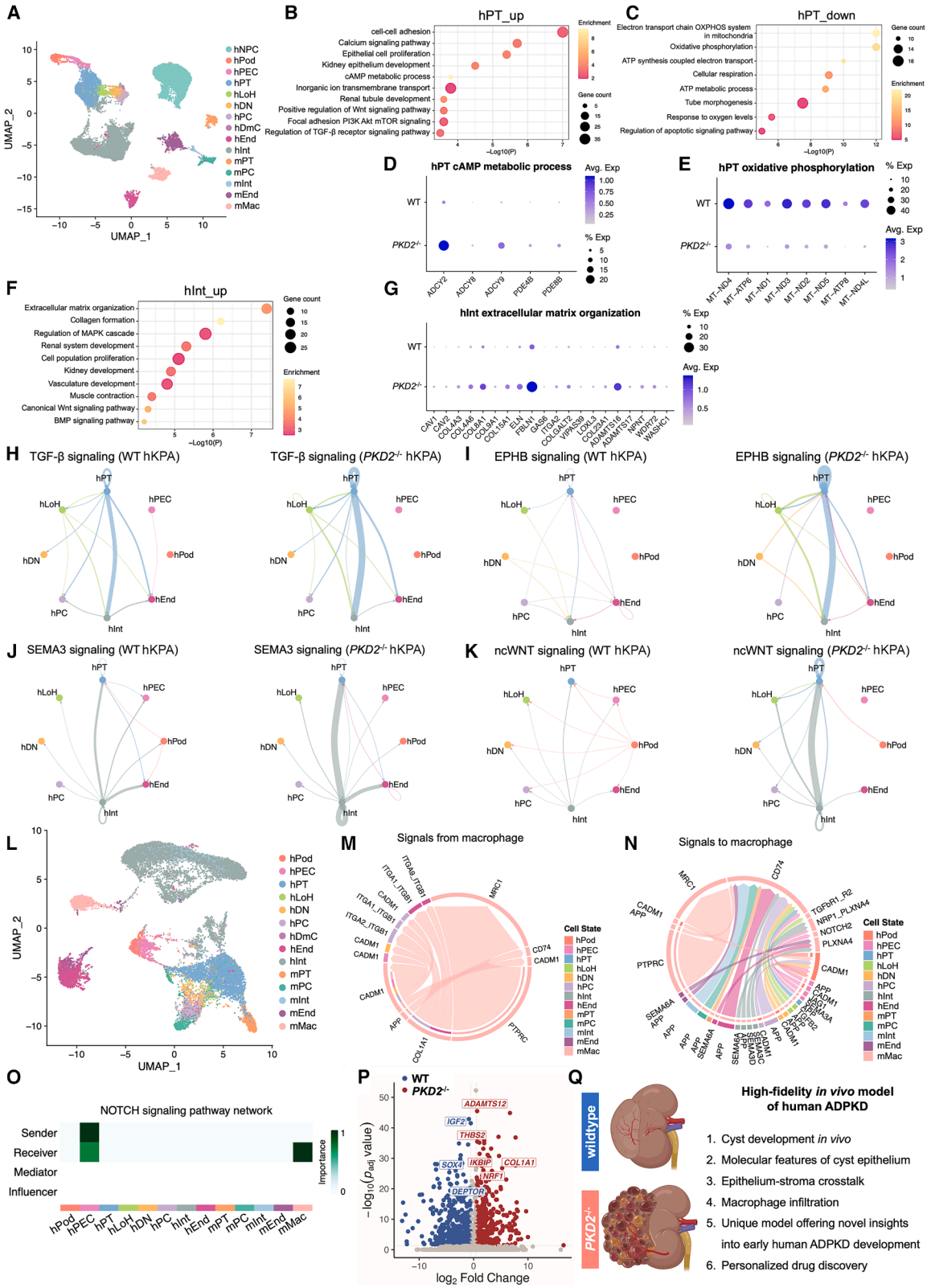

(legend on next page)

Materials availability

Cell lines, plasmids, and other unique resources generated in this study are available from the lead contact, Zhongwei Li (zhongwei.li@med.usc.edu), with a completed materials transfer agreement.

Data and code availability

Bulk RNA-seq data have been deposited at GEO (GEO: GSE264516). mKPA single-cell multiome data have been deposited at GEO (GEO: GSE262382). hKPA single-cell multiome data (*in vitro* culture) have been deposited at GEO (GEO: GSE272707). snRNA-seq data of day 6 hKPAs cultured with or without TTNPB have been deposited at GEO (GEO: GSE297771). snRNA-seq data of hKPA transplants (wild type and *PKD2*$^{-/-}$) have been deposited at GEO (GEO: GSE297772). This study does not report original code, and any additional information required to reanalyze the data reported in this paper is available from the lead contact upon request. Additional supplemental data have been deposited at Mendeley Data and are available at http://doi.org/10.17632/vs49gkxx95.1.

ACKNOWLEDGMENTS

We would like to thank the USC Flow Cytometry Facility, USC Optical Imaging Facility, USC Multi-Photon Microscopy Core, and USC Norris Medical Library Bioinformatics Service for data collection; the Xue-Ru Wu lab (Department of Urology, New York University) for providing the UPIIIb-C358 antibody; and Cristy Lytal for help with editing the manuscript. This work was supported by the NIH Director's Award (DP2DK135739), UKRO foundation funding, and the KSOM Dean's Pilot Award to Z. Li; NIH DK054364 and CZI seed network grant (CZIF2019-002430) to A.P.M.; NIH DK064324, DK123564, and DK135290 to J.P.-P.; and NIH DK136802 to N.O.L. Z.Z. was supported by a USC Stem Cell Challenge Award. P.M. was supported by NIH T32 training grant (T32HD060549). M.E.S. was supported by the CIRM Predoctoral Fellowship (EDUC4-12756). BioRender software was used to generate the graphical abstract and Figures 3D, 5A, and 7Q.

AUTHOR CONTRIBUTIONS

Conceptualization, B.H., P.M., and Z. Li; mKPA protocol development, B.H. and Z.Z.; *in vitro* hKPA protocol development, P.M. and B.H.; *in vivo* hKPA protocol development, B.H. and J.R.; bioinformatics analysis, J.H., S. Kim, Y.P., K.Z., B.H., S. Kumar, A.P.M., C.J., and Z. Li; methodology, investigation, and validation, B.H., Z.Z., P.M., K.K., C.C.Z., G.G., T.M., P.-E.Y.N., R.B., A. S., L.O., M.E.S., J.P., J.R., J.G., J.S., M.W.X., C.X., Z. Liu, and J.P.-P.; software and formal analysis, B.H., J.H., S. Kim, R.K.P., N.O.L., C.J., A.P.M., and Z. Li; resources, Z. Liu, C.E.M., D.E.-N., J.I., L.P., N.M.P.-S., K.R.H., and A.P.M.; writing—original draft, B.H., P.M., J.H., Z.Z., and Z. Li; writing—review and editing, B.H., P.M., J.H., Z.Z., N.O.L., N.M.P.-S., K.R.H., J.P.-P., C.J., A.P.M., and Z. Li.

DECLARATION OF INTERESTS

A.P.M. is a scientific advisor or consultant for eGENESIS, Trestle Biotherapeutics, GentiBio, and IVIVA Medical. J.P.-P. and G.G. are co-founders of Macula Densa Cell LLC, a biotechnology company that develops therapeutics to target macula densa cells for a regenerative treatment for chronic kidney disease. Macula Densa Cell LLC has a patent entitled "Targeting macula densa cells as a new therapeutic approach for kidney disease" (US patents 10,828,374 and 11,318,209). Z. Li, B.H., P.M., Z.Z., and A.P.M. have applied for intellectual property protection on technologies discussed here.

STAR★METHODS

Detailed methods are provided in the online version of this paper and include the following:

- KEY RESOURCES TABLE
- EXPERIMENTAL MODEL AND STUDY PARTICIPANT DETAILS
  - Human tissues
  - Mice
  - hPSC lines
- METHOD DETAILS
  - Optimization of mouse kidney explant culture conditions to identify v2 medium
  - Further development from v2 medium to v3 medium for hKPA culture
  - E12.5 mouse kidney *ex vivo* culture
  - Screening of additional factors supplemented into the "v2 medium"
  - Mouse NPC and UPC expansion
  - Generation of mKPA from expandable mouse NPCs and UPCs
  - Functional assays to assess various tubular and endocrine functions *in vitro*
  - Mouse Kidney Progenitor Assembloid transplantation into immunodeficient NSG mice
  - Human kidney progenitor assembloids transplantation into immunodeficient NSG mice
  - Intravital imaging using multiphoton microscopy (MPM)
  - Patch Clamp
  - Quantification and identification of urea and creatinine in cyst fluid collected from mKPAs and hKPAs transplant
  - iNPC and iUPC expansion
  - Generation of human kidney progenitor assembloids from expandable iNPCs and iUPCs
  - Bulk RNA sequencing
  - Bulk RNA-seq data analysis
  - Single nuclei isolation from kidney progenitor assembloid
  - snRNA-seq and snATAC-seq library construction and sequencing
  - Data analysis for snRNA-seq/snATAC-seq datasets

Figure 7. snRNA-seq analysis of *in vivo* ADPKD model sheds light on novel mechanisms

(A) UMAP visualization of cell clusters identified from the integrated snRNA-seq datasets of wild-type and *PKD2*$^{-/-}$ hKPA transplants.

(B and C) Gene Ontology (GO) enrichment analysis of upregulated genes (B) or downregulated genes (C) in the PT of *PKD2*$^{-/-}$ hKPA transplants compared with wild type.

(D and E) Dot plots showing the expression of genes related to cAMP metabolic process (D) and oxidative phosphorylation (E) in the PT of wild-type and *PKD2*$^{-/-}$ hKPA transplants.

(F) GO enrichment analysis of upregulated genes in the hInt of *PKD2*$^{-/-}$ hKPA transplants compared with wild type.

(G) Dot plots showing the expression of genes related to extracellular matrix organization in the hInt of wild-type and *PKD2*$^{-/-}$ hKPA transplants.

(H–K) Circle plot ligand-receptor analysis in wild-type (left) and *PKD2*$^{-/-}$ hKPA transplants (right) highlighting different signaling pathways identified.

(L) UMAP visualization of cell clusters identified upon integration of snRNA-seq datasets with the humanized mouse gene matrix and the human gene matrix in wild-type and *PKD2*$^{-/-}$ hKPA transplants.

(M and N) Chord diagrams depict gene-level signaling interactions involving macrophages (mMacro) inferred by CellChat. (M) Outgoing interactions from macrophages to other cell types. (N) Incoming interactions received by macrophages from other cell types. Each chord represents a ligand-receptor pair, colored by the interacting cell type.

(O) Heatmap of NOTCH signaling pathway network.

(P) Volcano plot showing DEGs in macrophages from wild-type and *PKD2*$^{-/-}$ hKPA transplants.

(Q) Summary of hKPA-based ADPKD modeling *in vivo*.

See also Figure S14.

- Immunofluorescence Staining
- RNAscope *in situ* hybridization
- TUNEL assay
- RNA isolation, reverse transcription and RT-qPCR

- QUANTIFICATION AND STATISTICAL ANALYSIS

SUPPLEMENTAL INFORMATION

Supplemental information can be found online at https://doi.org/10.1016/j.stem.2025.08.013.

Received: August 21, 2024
Revised: June 28, 2025
Accepted: August 22, 2025
Published: September 17, 2025

REFERENCES

1. Taguchi, A., Kaku, Y., Ohmori, T., Sharmin, S., Ogawa, M., Sasaki, H., and Nishinakamura, R. (2014). Redefining the in vivo origin of metanephric nephron progenitors enables generation of complex kidney structures from pluripotent stem cells. Cell Stem Cell *14*, 53–67. https://doi.org/10.1016/j.stem.2013.11.010.
2. Morizane, R., Lam, A.Q., Freedman, B.S., Kishi, S., Valerius, M.T., and Bonventre, J.V. (2015). Nephron organoids derived from human pluripotent stem cells model kidney development and injury. Nat. Biotechnol. *33*, 1193–1200. https://doi.org/10.1038/nbt.3392.
3. Kuraoka, S., Tanigawa, S., Taguchi, A., Hotta, A., Nakazato, H., Osafune, K., Kobayashi, A., and Nishinakamura, R. (2020). PKD1-Dependent Renal Cystogenesis in Human Induced Pluripotent Stem Cell-Derived Ureteric Bud/Collecting Duct Organoids. J. Am. Soc. Nephrol. *31*, 2355–2371. https://doi.org/10.1681/ASN.2020030378.
4. Takasato, M., Er, P.X., Chiu, H.S., Maier, B., Baillie, G.J., Ferguson, C., Parton, R.G., Wolvetang, E.J., Roost, M.S., Chuva de Sousa Lopes, S. M., et al. (2015). Kidney organoids from human iPS cells contain multiple lineages and model human nephrogenesis. Nature *526*, 564–568. https://doi.org/10.1038/nature15695.
5. Freedman, B.S., Brooks, C.R., Lam, A.Q., Fu, H., Morizane, R., Agrawal, V., Saad, A.F., Li, M.K., Hughes, M.R., Werff, R.V., et al. (2015). Modelling kidney disease with CRISPR-mutant kidney organoids derived from human pluripotent epiblast spheroids. Nat. Commun. *6*, 8715. https://doi.org/10.1038/ncomms9715.
6. Li, Z., Araoka, T., Wu, J., Liao, H.-K., Li, M., Lazo, M., Zhou, B., Sui, Y., Wu, M.-Z., Tamura, I., et al. (2016). 3D culture supports long-term expansion of mouse and human nephrogenic progenitors. Cell Stem Cell *19*, 516–529. https://doi.org/10.1016/j.stem.2016.07.016.
7. Przepiorski, A., Sander, V., Tran, T., Hollywood, J.A., Sorrenson, B., Shih, J.H., Wolvetang, E.J., McMahon, A.P., Holm, T.M., and Davidson, A.J. (2018). A Simple Bioreactor-Based Method to Generate Kidney Organoids from Pluripotent Stem Cells. Stem Cell Rep. *11*, 470–484. https://doi.org/10.1016/j.stemcr.2018.06.018.
8. Low, J.H., Li, P., Chew, E.G.Y., Zhou, B., Suzuki, K., Zhang, T., Lian, M. M., Liu, M., Aizawa, E., Rodriguez Esteban, C., et al. (2019). Generation of Human PSC-Derived Kidney Organoids with Patterned Nephron Segments and a De Novo Vascular Network. Cell Stem Cell *25*, 373–387.e9. https://doi.org/10.1016/j.stem.2019.06.009.
9. Garreta, E., Prado, P., Tarantino, C., Oria, R., Fanlo, L., Martí, E., Zalvidea, D., Trepat, X., Roca-Cusachs, P., Gavaldà-Navarro, A., et al. (2019). Fine tuning the extracellular environment accelerates the derivation of kidney organoids from human pluripotent stem cells. Nat. Mater. *18*, 397–405. https://doi.org/10.1038/s41563-019-0287-6.
10. Vanslambrouck, J.M., Wilson, S.B., Tan, K.S., Groenewegen, E., Rudraraju, R., Neil, J., Lawlor, K.T., Mah, S., Scurr, M., Howden, S.E., et al. (2022). Enhanced metanephric specification to functional proximal tubule enables toxicity screening and infectious disease modelling in kidney organoids. Nat. Commun. *13*, 5943. https://doi.org/10.1038/s41467-022-33623-z.
11. Huang, B., Zeng, Z., Kim, S., Fausto, C.C., Koppitch, K., Li, H., Li, Z., Chen, X., Guo, J., Zhang, C.C., et al. (2024). Long-term expandable mouse and human-induced nephron progenitor cells enable kidney organoid maturation and modeling of plasticity and disease. Cell Stem Cell *31*, 921–939.e17. https://doi.org/10.1016/j.stem.2024.04.002.
12. Mae, S.I., Ryosaka, M., Sakamoto, S., Matsuse, K., Nozaki, A., Igami, M., Kabai, R., Watanabe, A., and Osafune, K. (2020). Expansion of Human iPSC-Derived Ureteric Bud Organoids with Repeated Branching Potential. Cell Rep. *32*, 107963. https://doi.org/10.1016/j.celrep.2020.107963.
13. Howden, S.E., Wilson, S.B., Groenewegen, E., Starks, L., Forbes, T.A., Tan, K.S., Vanslambrouck, J.M., Holloway, E.M., Chen, Y.H., Jain, S., et al. (2021). Plasticity of distal nephron epithelia from human kidney organoids enables the induction of ureteric tip and stalk. Cell Stem Cell *28*, 671–684.e6. https://doi.org/10.1016/j.stem.2020.12.001.
14. Zeng, Z., Huang, B., Parvez, R.K., Li, Y., Chen, J., Vonk, A.C., Thornton, M.E., Patel, T., Rutledge, E.A., Kim, A.D., et al. (2021). Generation of patterned kidney organoids that recapitulate the adult kidney collecting duct system from expandable ureteric bud progenitors. Nat. Commun. *12*, 3641. https://doi.org/10.1038/s41467-021-23911-5.
15. Shi, M., McCracken, K.W., Patel, A.B., Zhang, W., Ester, L., Valerius, M. T., and Bonventre, J.V. (2023). Human ureteric bud organoids recapitulate branching morphogenesis and differentiate into functional collecting duct cell types. Nat. Biotechnol. *41*, 252–261. https://doi.org/10.1038/s41587-022-01429-5.
16. Wu, H., Uchimura, K., Donnelly, E.L., Kirita, Y., Morris, S.A., and Humphreys, B.D. (2018). Comparative Analysis and Refinement of Human PSC-Derived Kidney Organoid Differentiation with Single-Cell Transcriptomics. Cell Stem Cell *23*, 869–881.e8. https://doi.org/10.1016/j.stem.2018.10.010.
17. Subramanian, A., Sidhom, E.H., Emani, M., Vernon, K., Sahakian, N., Zhou, Y., Kost-Alimova, M., Slyper, M., Waldman, J., Dionne, D., et al. (2019). Single cell census of human kidney organoids shows reproducibility and diminished off-target cells after transplantation. Nat. Commun. *10*, 5462. https://doi.org/10.1038/s41467-019-13382-0.
18. Phipson, B., Er, P.X., Combes, A.N., Forbes, T.A., Howden, S.E., Zappia, L., Yen, H.J., Lawlor, K.T., Hale, L.J., Sun, J., et al. (2019). Evaluation of variability in human kidney organoids. Nat. Methods *16*, 79–87. https://doi.org/10.1038/s41592-018-0253-2.
19. Yoshimura, Y., Muto, Y., Ledru, N., Wu, H., Omachi, K., Miner, J.H., and Humphreys, B.D. (2023). A single-cell multiomic analysis of kidney organoid differentiation. Proc. Natl. Acad. Sci. USA *120*, e2219699120. https://doi.org/10.1073/pnas.2219699120.
20. Ransick, A., Lindström, N.O., Liu, J., Zhu, Q., Guo, J.J., Alvarado, G.F., Kim, A.D., Black, H.G., Kim, J., and McMahon, A.P. (2019). Single-Cell Profiling Reveals Sex, Lineage, and Regional Diversity in the Mouse Kidney. Dev. Cell *51*, 399–413.e7. https://doi.org/10.1016/j.devcel.2019.10.005.
21. Park, J., Shrestha, R., Qiu, C., Kondo, A., Huang, S., Werth, M., Li, M., Barasch, J., and Suszták, K. (2018). Single-cell transcriptomics of the mouse kidney reveals potential cellular targets of kidney disease. Science *360*, 758–763. https://doi.org/10.1126/science.aar2131.
22. Muto, Y., Wilson, P.C., Ledru, N., Wu, H., Dimke, H., Waikar, S.S., and Humphreys, B.D. (2021). Single cell transcriptional and chromatin accessibility profiling redefine cellular heterogeneity in the adult human kidney. Nat. Commun. *12*, 2190. https://doi.org/10.1038/s41467-021-22368-w.
23. McMahon, A.P. (2016). Development of the mammalian kidney. Curr. Top. Dev. Biol. *117*, 31–64. https://doi.org/10.1016/bs.ctdb.2015.10.010.
24. Combes, A.N., Davies, J.A., and Little, M.H. (2015). Cell-cell interactions driving kidney morphogenesis. Curr. Top. Dev. Biol. *112*, 467–508. https://doi.org/10.1016/bs.ctdb.2014.12.002.

25. Kobayashi, A., Valerius, M.T., Mugford, J.W., Carroll, T.J., Self, M., Oliver, G., and McMahon, A.P. (2008). Six2 defines and regulates a multipotent self-renewing nephron progenitor population throughout mammalian kidney development. Cell Stem Cell *3*, 169–181. https://doi.org/10.1016/j.stem.2008.05.020.

26. Rutledge, E.A., Benazet, J.D., and McMahon, A.P. (2017). Cellular heterogeneity in the ureteric progenitor niche and distinct profiles of branching morphogenesis in organ development. Development *144*, 3177–3188. https://doi.org/10.1242/dev.149112.

27. Schnell, J., Achieng, M., and Lindström, N.O. (2022). Principles of human and mouse nephron development. Nat. Rev. Nephrol. *18*, 628–642. https://doi.org/10.1038/s41581-022-00598-5.

28. Costantini, F. (2012). Genetic controls and cellular behaviors in branching morphogenesis of the renal collecting system. Wiley Interdiscip. Rev. Dev. Biol. *1*, 693–713. https://doi.org/10.1002/wdev.52.

29. Kobayashi, A., Mugford, J.W., Krautzberger, A.M., Naiman, N., Liao, J., and McMahon, A.P. (2014). Identification of a multipotent self-renewing stromal progenitor population during mammalian kidney organogenesis. Stem Cell Rep. *3*, 650–662. https://doi.org/10.1016/j.stemcr.2014.08.008.

30. Ryan, A.R., and Cleaver, O. (2022). Plumbing our organs: Lessons from vascular development to instruct lab generated tissues. Curr. Top. Dev. Biol. *148*, 165–194. https://doi.org/10.1016/bs.ctdb.2022.02.013.

31. Brown, A.C., Muthukrishnan, S.D., and Oxburgh, L. (2015). A synthetic niche for nephron progenitor cells. Dev. Cell *34*, 229–241. https://doi.org/10.1016/j.devcel.2015.06.021.

32. Tanigawa, S., Taguchi, A., Sharma, N., Perantoni, A.O., and Nishinakamura, R. (2016). Selective In Vitro Propagation of Nephron Progenitors Derived from Embryos and Pluripotent Stem Cells. Cell Rep. *15*, 801–813. https://doi.org/10.1016/j.celrep.2016.03.076.

33. Taguchi, A., and Nishinakamura, R. (2017). Higher-order kidney organogenesis from pluripotent stem cells. Cell Stem Cell *21*, 730–746.e6. https://doi.org/10.1016/j.stem.2017.10.011.

34. Mae, S.I., Ryosaka, M., Toyoda, T., Matsuse, K., Oshima, Y., Tsujimoto, H., Okumura, S., Shibasaki, A., and Osafune, K. (2018). Generation of branching ureteric bud tissues from human pluripotent stem cells. Biochem. Biophys. Res. Commun. *495*, 954–961. https://doi.org/10.1016/j.bbrc.2017.11.105.

35. Tanigawa, S., Tanaka, E., Miike, K., Ohmori, T., Inoue, D., Cai, C.-L., Taguchi, A., Kobayashi, A., and Nishinakamura, R. (2022). Generation of the organotypic kidney structure by integrating pluripotent stem cell-derived renal stroma. Nat. Commun. *13*, 611. https://doi.org/10.1038/s41467-022-28226-7.

36. Palakkan, A.A., Tarnick, J., Waterfall, M., Sallam, M., Glykofrydis, F., Elhendawi, M., and Davies, J.A. (2022). Production of kidney organoids arranged around single ureteric bud trees, and containing endogenous blood vessels, solely from embryonic stem cells. Sci. Rep. *12*, 12573. https://doi.org/10.1038/s41598-022-16768-1.

37. Tsujimoto, H., Kasahara, T., Sueta, S.I., Araoka, T., Sakamoto, S., Okada, C., Mae, S.I., Nakajima, T., Okamoto, N., Taura, D., et al. (2020). A Modular Differentiation System Maps Multiple Human Kidney Lineages from Pluripotent Stem Cells. Cell Rep. *31*, 107476. https://doi.org/10.1016/j.celrep.2020.03.040.

38. Uchimura, K., Wu, H., Yoshimura, Y., and Humphreys, B.D. (2020). Human Pluripotent Stem Cell-Derived Kidney Organoids with Improved Collecting Duct Maturation and Injury Modeling. Cell Rep. *33*, 108514. https://doi.org/10.1016/j.celrep.2020.108514.

39. Porter, C.M., Qian, G.C., Grindel, S.H., and Hughes, A.J. (2024). Highly parallel production of designer organoids by mosaic patterning of progenitors. Cell Syst. *15*, 649–661.e9. https://doi.org/10.1016/j.cels.2024.06.004.

40. Shi, M., Crouse, B., Sundaram, N., Pode Shakked, N., Thorner, K., King, N.M., Dutta, P., Ester, L., Zhang, W., Govindarajah, V., et al. (2025). Integrating collecting systems in human kidney organoids through fusion of distal nephron to ureteric bud. Cell Stem Cell *32*, 1055–1070.e8. https://doi.org/10.1016/j.stem.2025.04.008.

41. Wilson, S.B., Santos, I.P., Wildfang, L., Imsa, K., and Little, M.H. (2025). Generation of multi-lineage kidney assembloids with integration between nephrons and a single exiting collecting duct. Preprint at bioRxiv. https://doi.org/10.1101/2025.02.27.640561.

42. Neary, J.P., Singh, J., Bishop, S.A., Dech, R.T., Butz, M.J.A., and Len, T.K. (2019). An Evidence-Based Objective Study Protocol for Evaluating Cardiovascular and Cerebrovascular Indices Following Concussion: The Neary Protocol. Methods Protoc. *2*, 23. https://doi.org/10.3390/mps2010023.

43. England, A.R., Chaney, C.P., Das, A., Patel, M., Malewska, A., Armendariz, D., Hon, G.C., Strand, D.W., Drake, K.A., and Carroll, T.J. (2020). Identification and characterization of cellular heterogeneity within the developing renal interstitium. Development *147*, dev190108. https://doi.org/10.1242/dev.190108.

44. Naganuma, H., Miike, K., Ohmori, T., Tanigawa, S., Ichikawa, T., Yamane, M., Eto, M., Niwa, H., Kobayashi, A., and Nishinakamura, R. (2021). Molecular detection of maturation stages in the developing kidney. Dev. Biol. *470*, 62–73. https://doi.org/10.1016/j.ydbio.2020.11.002.

45. Chi, X., Hadjantonakis, A.K., Wu, Z., Hyink, D., and Costantini, F. (2009). A transgenic mouse that reveals cell shape and arrangement during ureteric bud branching. Genesis *47*, 61–66. https://doi.org/10.1002/dvg.20452.

46. Combes, A.N., Phipson, B., Lawlor, K.T., Dorison, A., Patrick, R., Zappia, L., Harvey, R.P., Oshlack, A., and Little, M.H. (2019). Single cell analysis of the developing mouse kidney provides deeper insight into marker gene expression and ligand-receptor crosstalk. Development *146*, dev178673. https://doi.org/10.1242/dev.178673.

47. Kim, S., Koppitch, K., Parvez, R.K., Guo, J., Achieng, M., Schnell, J., Lindström, N.O., and McMahon, A.P. (2024). Comparative single-cell analyses identify shared and divergent features of human and mouse kidney development. Dev. Cell *59*, 2912–2930.e7. https://doi.org/10.1016/j.devcel.2024.07.013.

48. Dresser, M.J., Leabman, M.K., and Giacomini, K.M. (2001). Transporters involved in the elimination of drugs in the kidney: organic anion transporters and organic cation transporters. J. Pharm. Sci. *90*, 397–421. https://doi.org/10.1002/1520-6017(200104)90:4<397::aid-jps1000>3.0.co;2-d.

49. Lawrence, M.L., Chang, C.-H., and Davies, J.A. (2015). Transport of organic anions and cations in murine embryonic kidney development and in serially-reaggregated engineered kidneys. Sci. Rep. *5*, 9092. https://doi.org/10.1038/srep09092.

50. Zhao, G., Meier, T.I., Kahl, S.D., Gee, K.R., and Blaszczak, L.C. (1999). BOCILLIN FL, a sensitive and commercially available reagent for detection of penicillin-binding proteins. Antimicrob. Agents Chemother. *43*, 1124–1128. https://doi.org/10.1128/AAC.43.5.1124.

51. O'Callaghan, C. (2016). The Renal System at a Glance (John Wiley & Sons).

52. Shankar, A.S., Du, Z., Mora, H.T., van den Bosch, T.P.P., Korevaar, S.S., Van den Berg-Garrelds, I.M., Bindels, E., Lopez-Iglesias, C., Clahsen-van Groningen, M.C., Gribnau, J., et al. (2021). Human kidney organoids produce functional renin. Kidney Int. *99*, 134–147. https://doi.org/10.1016/j.kint.2020.08.008.

53. Hammerman, M.R. (2004). Renal organogenesis from transplanted metanephric primordia. J. Am. Soc. Nephrol. *15*, 1126–1132. https://doi.org/10.1097/01.asn.0000106020.64930.64.

54. Rogers, S.A., and Hammerman, M.R. (2004). Prolongation of life in anephric rats following de novo renal organogenesis. Organogenesis *1*, 22–25. https://doi.org/10.4161/org.1.1.1009.

55. Rogers, S.A., and Hammerman, M.R. (2001). Transplantation of rat metanephroi into mice. Am. J. Physiol. Regul. Integr. Comp. Physiol. *280*, R1865–R1869. https://doi.org/10.1152/ajpregu.2001.280.6.R1865.

56. Rogers, S.A., Lowell, J.A., Hammerman, N.A., and Hammerman, M.R. (1998). Transplantation of developing metanephroi into adult rats. Kidney Int. *54*, 27–37. https://doi.org/10.1046/j.1523-1755.1998.00971.x.

57. Marshall, D., Dilworth, M.R., Clancy, M., Bravery, C.A., and Ashton, N. (2007). Increasing renal mass improves survival in anephric rats following metanephros transplantation. Exp. Physiol. *92*, 263–271. https://doi.org/10.1113/expphysiol.2006.036319.

58. Dekel, B., Burakova, T., Arditti, F.D., Reich-Zeliger, S., Milstein, O., Aviel-Ronen, S., Rechavi, G., Friedman, N., Kaminski, N., Passwell, J.H., et al. (2003). Human and porcine early kidney precursors as a new source for transplantation. Nat. Med. *9*, 53–60. https://doi.org/10.1038/nm812.

59. Yokote, S., Matsunari, H., Iwai, S., Yamanaka, S., Uchikura, A., Fujimoto, E., Matsumoto, K., Nagashima, H., Kobayashi, E., and Yokoo, T. (2015). Urine excretion strategy for stem cell-generated embryonic kidneys. Proc. Natl. Acad. Sci. USA *112*, 12980–12985. https://doi.org/10.1073/pnas.1507803112.

60. Kinoshita, Y., Kobayashi, E., Matsui, K., Inage, Y., Morimoto, K., Yamamoto, S., Iwai, S., Kitada, K., Iwasawa, K., Saito, Y., et al. (2025). Life-supporting functional kidney replacement by integration of embryonic metanephros-bladder composite tissue transplants. Kidney Int. *107*, 1051–1063. https://doi.org/10.1016/j.kint.2025.02.024.

61. Lindström, N.O., Tran, T., Guo, J., Rutledge, E., Parvez, R.K., Thornton, M.E., Grubbs, B., McMahon, J.A., and McMahon, A.P. (2018). Conserved and divergent molecular and anatomic features of human and mouse nephron patterning. J. Am. Soc. Nephrol. *29*, 825–840. https://doi.org/10.1681/ASN.2017091036.

62. Koseki, C., Herzlinger, D., and Al-Awqati, Q. (1992). Apoptosis in metanephric development. J. Cell Biol. *119*, 1327–1333. https://doi.org/10.1083/jcb.119.5.1327.

63. Barasch, J., Qiao, J., McWilliams, G., Chen, D., Oliver, J.A., and Herzlinger, D. (1997). Ureteric bud cells secrete multiple factors, including bFGF, which rescue renal progenitors from apoptosis. Am. J. Physiol. *273*, F757–F767. https://doi.org/10.1152/ajprenal.1997.273.5.F757.

64. Lindström, N.O., Sealfon, R., Chen, X., Parvez, R.K., Ransick, A., De Sena Brandine, G., Guo, J., Hill, B., Tran, T., Kim, A.D., et al. (2021). Spatial transcriptional mapping of the human nephrogenic program. Dev. Cell *56*, 2381–2398.e6. https://doi.org/10.1016/j.devcel.2021.07.017.

65. Kispert, A., Vainio, S., and McMahon, A.P. (1998). Wnt-4 is a mesenchymal signal for epithelial transformation of metanephric mesenchyme in the developing kidney. Development *125*, 4225–4234. https://doi.org/10.1242/dev.125.21.4225.

66. Carroll, T.J., Park, J.S., Hayashi, S., Majumdar, A., and McMahon, A.P. (2005). Wnt9b plays a central role in the regulation of mesenchymal to epithelial transitions underlying organogenesis of the mammalian urogenital system. Dev. Cell *9*, 283–292. https://doi.org/10.1016/j.devcel.2005.05.016.

67. Park, J.S., Valerius, M.T., and McMahon, A.P. (2007). Wnt/beta-catenin signaling regulates nephron induction during mouse kidney development. Development *134*, 2533–2539. https://doi.org/10.1242/dev.006155.

68. Tanigawa, S., Wang, H., Yang, Y., Sharma, N., Tarasova, N., Ajima, R., Yamaguchi, T.P., Rodriguez, L.G., and Perantoni, A.O. (2011). Wnt4 induces nephronic tubules in metanephric mesenchyme by a non-canonical mechanism. Dev. Biol. *352*, 58–69. https://doi.org/10.1016/j.ydbio.2011.01.012.

69. Tran, T., Lindström, N.O., Ransick, A., De Sena Brandine, G., Guo, Q., Kim, A.D., Der, B., Peti-Peterdi, J., Smith, A.D., Thornton, M., et al. (2019). In Vivo Developmental Trajectories of Human Podocyte Inform In Vitro Differentiation of Pluripotent Stem Cell-Derived Podocytes. Dev. Cell *50*, 102–116.e6. https://doi.org/10.1016/j.devcel.2019.06.001.

70. Hudson, B.G., Tryggvason, K., Sundaramoorthy, M., and Neilson, E.G. (2003). Alport's syndrome, Goodpasture's syndrome, and type IV collagen. N. Engl. J. Med. *348*, 2543–2556. https://doi.org/10.1056/NEJMra022296.

71. Kruegel, J., Rubel, D., and Gross, O. (2013). Alport syndrome–insights from basic and clinical research. Nat. Rev. Nephrol. *9*, 170–178. https://doi.org/10.1038/nrneph.2012.259.

72. Hoxha, E., Reinhard, L., and Stahl, R.A.K. (2022). Membranous nephropathy: new pathogenic mechanisms and their clinical implications. Nat. Rev. Nephrol. *18*, 466–478. https://doi.org/10.1038/s41581-022-00564-1.

73. Bhargava, P., and Schnellmann, R.G. (2017). Mitochondrial energetics in the kidney. Nat. Rev. Nephrol. *13*, 629–646. https://doi.org/10.1038/nrneph.2017.107.

74. Bergmann, C., Guay-Woodford, L.M., Harris, P.C., Horie, S., Peters, D.J.M., and Torres, V.E. (2018). Polycystic kidney disease. Nat. Rev. Dis. Primers *4*, 50. https://doi.org/10.1038/s41572-018-0047-y.

75. Cruz, N.M., Song, X., Czerniecki, S.M., Gulieva, R.E., Churchill, A.J., Kim, Y.K., Winston, K., Tran, L.M., Diaz, M.A., Fu, H., et al. (2017). Organoid cystogenesis reveals a critical role of microenvironment in human polycystic kidney disease. Nat. Mater. *16*, 1112–1119. https://doi.org/10.1038/nmat4994.

76. Czerniecki, S.M., Cruz, N.M., Harder, J.L., Menon, R., Annis, J., Otto, E.A., Gulieva, R.E., Islas, L.V., Kim, Y.K., Tran, L.M., et al. (2018). High-Throughput Screening Enhances Kidney Organoid Differentiation from Human Pluripotent Stem Cells and Enables Automated Multidimensional Phenotyping. Cell Stem Cell *22*, 929–940.e4. https://doi.org/10.1016/j.stem.2018.04.022.

77. Reiter, J.F., and Leroux, M.R. (2017). Genes and molecular pathways underpinning ciliopathies. Nat. Rev. Mol. Cell Biol. *18*, 533–547. https://doi.org/10.1038/nrm.2017.60.

78. Anvarian, Z., Mykytyn, K., Mukhopadhyay, S., Pedersen, L.B., and Christensen, S.T. (2019). Cellular signalling by primary cilia in development, organ function and disease. Nat. Rev. Nephrol. *15*, 199–219. https://doi.org/10.1038/s41581-019-0116-9.

79. Song, C.J., Zimmerman, K.A., Henke, S.J., and Yoder, B.K. (2017). Inflammation and Fibrosis in Polycystic Kidney Disease. Results Probl. Cell Differ. *60*, 323–344. https://doi.org/10.1007/978-3-319-51436-9_12.

80. Cassini, M.F., Kakade, V.R., Kurtz, E., Sulkowski, P., Glazer, P., Torres, R., Somlo, S., and Cantley, L.G. (2018). Mcp1 Promotes Macrophage-Dependent Cyst Expansion in Autosomal Dominant Polycystic Kidney Disease. J. Am. Soc. Nephrol. *29*, 2471–2481. https://doi.org/10.1681/ASN.2018050518.

81. Chen, L., Zhou, X., Fan, L.X., Yao, Y., Swenson-Fields, K.I., Gadjeva, M., Wallace, D.P., Peters, D.J.M., Yu, A., Grantham, J.J., et al. (2015). Macrophage migration inhibitory factor promotes cyst growth in polycystic kidney disease. J. Clin. Invest. *125*, 2399–2412. https://doi.org/10.1172/JCI80467.

82. Karihaloo, A., Koraishy, F., Huen, S.C., Lee, Y., Merrick, D., Caplan, M.J., Somlo, S., and Cantley, L.G. (2011). Macrophages promote cyst growth in polycystic kidney disease. J. Am. Soc. Nephrol. *22*, 1809–1814. https://doi.org/10.1681/ASN.2011010084.

83. Swenson-Fields, K.I., Vivian, C.J., Salah, S.M., Peda, J.D., Davis, B.M., van Rooijen, N., Wallace, D.P., and Fields, T.A. (2013). Macrophages promote polycystic kidney disease progression. Kidney Int. *83*, 855–864. https://doi.org/10.1038/ki.2012.446.

84. Zimmerman, K.A., Huang, J., He, L., Revell, D.Z., Li, Z., Hsu, J.S., Fitzgibbon, W.R., Hazard, E.S., Hardiman, G., Mrug, M., et al. (2020). Interferon Regulatory Factor-5 in Resident Macrophage Promotes Polycystic Kidney Disease. Kidney360 *1*, 179–190. https://doi.org/10.34067/KID.0001052019.

85. Muto, Y., Dixon, E.E., Yoshimura, Y., Wu, H., Omachi, K., Ledru, N., Wilson, P.C., King, A.J., Eric Olson, N., Gunawan, M.G., et al. (2022). Defining cellular complexity in human autosomal dominant polycystic kidney disease by multimodal single cell analysis. Nat. Commun. *13*, 6497. https://doi.org/10.1038/s41467-022-34255-z.

86. Jin, S., Guerrero-Juarez, C.F., Zhang, L., Chang, I., Ramos, R., Kuan, C. H., Myung, P., Plikus, M.V., and Nie, Q. (2021). Inference and analysis of cell-cell communication using CellChat. Nat. Commun. *12*, 1088. https://doi.org/10.1038/s41467-021-21246-9.

87. Hoeft, K., Schaefer, G.J.L., Kim, H., Schumacher, D., Bleckwehl, T., Long, Q., Klinkhammer, B.M., Peisker, F., Koch, L., Nagai, J., et al. (2023). Platelet-instructed SPP1^{+} macrophages drive myofibroblast activation in fibrosis in a CXCL4-dependent manner. Cell Rep. *42*, 112131. https://doi.org/10.1016/j.celrep.2023.112131.

88. Cai, A., Ye, G., Placier, S., Frère, P., Surin, B., Vandermeersch, S., Kormann, R., Xu-Dubois, Y.C., Genest, M., Lannoy, M., et al. (2022). Genetic inactivation of Semaphorin 3C protects mice from acute kidney injury. Kidney Int. *101*, 720–732. https://doi.org/10.1016/j.kint.2021.12.028.

89. Sang, Y., Tsuji, K., Fukushima, K., Takahashi, K., Kitamura, S., and Wada, J. (2021). Semaporin3A inhibitor ameliorates renal fibrosis through the regulation of JNK signaling. Am. J. Physiol. Ren. Physiol. *321*, F740–F756. https://doi.org/10.1152/ajprenal.00234.2021.

90. Xia, J., and Worzfeld, T. (2016). Semaphorins and Plexins in Kidney Disease. Nephron *132*, 93–100. https://doi.org/10.1159/000443645.

91. Foo, S.S., Turner, C.J., Adams, S., Compagni, A., Aubyn, D., Kogata, N., Lindblom, P., Shani, M., Zicha, D., and Adams, R.H. (2006). Ephrin-B2 controls cell motility and adhesion during blood-vessel-wall assembly. Cell *124*, 161–173. https://doi.org/10.1016/j.cell.2005.10.034.

92. Ren, S., and Duffield, J.S. (2013). Pericytes in kidney fibrosis. Curr. Opin. Nephrol. Hypertens. *22*, 471–480. https://doi.org/10.1097/MNH.0b013e328362485e.

93. Dubin, R.F., Deo, R., Ren, Y., Wang, J., Zheng, Z., Shou, H., Go, A.S., Parsa, A., Lash, J.P., Rahman, M., et al. (2023). Proteomics of CKD progression in the chronic renal insufficiency cohort. Nat. Commun. *14*, 6340. https://doi.org/10.1038/s41467-023-41642-7.

94. Lienkamp, S.S., Liu, K., Karner, C.M., Carroll, T.J., Ronneberger, O., Wallingford, J.B., and Walz, G. (2012). Vertebrate kidney tubules elongate using a planar cell polarity-dependent, rosette-based mechanism of convergent extension. Nat. Genet. *44*, 1382–1387. https://doi.org/10.1038/ng.2452.

95. Malik, S.A., Modarage, K., and Goggolidou, P. (2020). The Role of Wnt Signalling in Chronic Kidney Disease (CKD). Genes (Basel) *11*, 496. https://doi.org/10.3390/genes11050496.

96. Richards, T., Modarage, K., Dean, C., McCarthy-Boxer, A., Hilton, H., Esapa, C., Norman, J., Wilson, P., and Goggolidou, P. (2019). Atmin modulates Pkhd1 expression and may mediate Autosomal Recessive Polycystic Kidney Disease (ARPKD) through altered non-canonical Wnt/Planar Cell Polarity (PCP) signalling. Biochim. Biophys. Acta Mol. Basis Dis. *1865*, 378–390. https://doi.org/10.1016/j.bbadis.2018.11.003.

97. Zimmerman, K.A., Hopp, K., and Mrug, M. (2020). Role of chemokines, innate and adaptive immunity. Cell. Signal. *73*, 109647. https://doi.org/10.1016/j.cellsig.2020.109647.

98. Durinck, S., Moreau, Y., Kasprzyk, A., Davis, S., De Moor, B., Brazma, A., and Huber, W. (2005). BioMart and Bioconductor: a powerful link between biological databases and microarray data analysis. Bioinformatics *21*, 3439–3440. https://doi.org/10.1093/bioinformatics/bti525.

99. Durinck, S., Spellman, P.T., Birney, E., and Huber, W. (2009). Mapping identifiers for the integration of genomic datasets with the R/Bioconductor package biomaRt. Nat. Protoc. *4*, 1184–1191. https://doi.org/10.1038/nprot.2009.97.

100. Hao, Y., Stuart, T., Kowalski, M.H., Choudhary, S., Hoffman, P., Hartman, A., Srivastava, A., Molla, G., Madad, S., Fernandez-Granda, C., et al. (2024). Dictionary learning for integrative, multimodal and scalable single-cell analysis. Nat. Biotechnol. *42*, 293–304. https://doi.org/10.1038/s41587-023-01767-y.

101. Foldi, J., Chung, A.Y., Xu, H., Zhu, J., Outtz, H.H., Kitajewski, J., Li, Y., Hu, X., and Ivashkiv, L.B. (2010). Autoamplification of Notch signaling in macrophages by TLR-induced and RBP-J-dependent induction of Jagged1. J. Immunol. *185*, 5023–5031. https://doi.org/10.4049/jimmunol.1001544.

102. Zimmerman, K.A., Huang, J., He, L., Revell, D.Z., Li, Z., Hsu, J.-S., Fitzgibbon, W.R., Hazard, E.S., Hardiman, G., Mrug, M., et al. (2020). Interferon Regulatory Factor 5 in Resident Macrophage Promotes Polycystic Kidney Disease. Kidney360 *1*, 179–190. https://doi.org/10.34067/KID.0001052019.

103. Li, X., Magenheimer, B.S., Xia, S., Johnson, T., Wallace, D.P., Calvet, J. P., and Li, R. (2008). A tumor necrosis factor-alpha-mediated pathway promoting autosomal dominant polycystic kidney disease. Nat. Med. *14*, 863–868. https://doi.org/10.1038/nm1783.

104. Tran, T., Song, C.J., Nguyen, T., Cheng, S.Y., McMahon, J.A., Yang, R., Guo, Q., Der, B., Lindström, N.O., Lin, D.C.H., et al. (2022). A scalable organoid model of human autosomal dominant polycystic kidney disease for disease mechanism and drug discovery. Cell Stem Cell *29*, 1083–1101.e7. https://doi.org/10.1016/j.stem.2022.06.005.

105. Shimizu, T., Mae, S.I., Araoka, T., Okita, K., Hotta, A., Yamagata, K., and Osafune, K. (2020). A novel ADPKD model using kidney organoids derived from disease-specific human iPSCs. Biochem. Biophys. Res. Commun. *529*, 1186–1194. https://doi.org/10.1016/j.bbrc.2020.06.141.

106. Liu, M., Zhang, C., Gong, X., Zhang, T., Lian, M.M., Chew, E.G.Y., Cardilla, A., Suzuki, K., Wang, H., Yuan, Y., et al. (2024). Kidney organoid models reveal cilium-autophagy metabolic axis as a therapeutic target for PKD both in vitro and in vivo. Cell Stem Cell *31*, 52–70.e8. https://doi.org/10.1016/j.stem.2023.12.003.

107. Lindström, N.O., McMahon, J.A., Guo, J., Tran, T., Guo, Q., Rutledge, E., Parvez, R.K., Saribekyan, G., Schuler, R.E., Liao, C., et al. (2018). Conserved and divergent features of human and mouse kidney organogenesis. J. Am. Soc. Nephrol. *29*, 785–805. https://doi.org/10.1681/ASN.2017080887.

108. Lindström, N.O., Guo, J., Kim, A.D., Tran, T., Guo, Q., De Sena Brandine, G.D.S., Ransick, A., Parvez, R.K., Thornton, M.E., Baskin, L., et al. (2018). Conserved and divergent features of mesenchymal progenitor cell types within the cortical nephrogenic niche of the human and mouse kidney. J. Am. Soc. Nephrol. *29*, 806–824. https://doi.org/10.1681/ASN.2017080890.

109. Schneider, C.A., Rasband, W.S., and Eliceiri, K.W. (2012). NIH Image to ImageJ: 25 years of image analysis. Nat. Methods *9*, 671–675. https://doi.org/10.1038/nmeth.2089.

110. Grobstein, C. (1953). Epithelio-mesenchymal specificity in the morphogenesis of mouse sub-mandibular rudiments in vitro. J. Exp. Zool. *124*, 383–413. https://doi.org/10.1002/jez.1401240211.

111. Schiessl, I.M., Fremter, K., Burford, J.L., Castrop, H., and Peti-Peterdi, J. (2020). Long-term cell fate tracking of individual renal cells using serial intravital microscopy. Imaging and Tracking Stem Cells. Methods Mol. Biol. *2150*, 25–44.

112. Gyarmati, G., Shroff, U.N., Riquier-Brison, A., Desposito, D., Ju, W., Stocker, S.D., Izuhara, A., Deepak, S., Becerra Calderon, A.B., Burford, J.L., et al. (2024). Neuronally differentiated macula densa cells regulate tissue remodeling and regeneration in the kidney. J. Clin. Invest. *134*, e174558. https://doi.org/10.1172/JCI174558.

113. Kang, J.J., Toma, I., Sipos, A., McCulloch, F., and Peti-Peterdi, J. (2006). Quantitative imaging of basic functions in renal (patho)physiology. Am. J. Physiol. Renal Physiol. *291*, F495–F502. https://doi.org/10.1152/ajprenal.00521.2005.

114. Isaeva, E., Bohovyk, R., Fedoriuk, M., Shalygin, A., Klemens, C.A., Zietara, A., Levchenko, V., Denton, J.S., Staruschenko, A., and Palygin, O. (2022). Crosstalk between epithelial sodium channels (ENaC) and basolateral potassium channels (Kir 4.1/Kir 5.1) in the cortical collecting duct. Br. J. Pharmacol. *179*, 2953–2968. https://doi.org/10.1111/bph.15779.

115. Zhou, Y., Zhou, B., Pache, L., Chang, M., Khodabakhshi, A.H., Tanaseichuk, O., Benner, C., and Chanda, S.K. (2019). Metascape provides a biologist-oriented resource for the analysis of systems-level

datasets. Nat. Commun. *10*, 1523. https://doi.org/10.1038/s41467-019-09234-6.

116. Xu, S., Hu, E., Cai, Y., Xie, Z., Luo, X., Zhan, L., Tang, W., Wang, Q., Liu, B., Wang, R., et al. (2024). Using clusterProfiler to characterize multiomics data. Nat. Protoc. *19*, 3292–3320. https://doi.org/10.1038/s41596-024-01020-z.

117. Korsunsky, I., Millard, N., Fan, J., Slowikowski, K., Zhang, F., Wei, K., Baglaenko, Y., Brenner, M., Loh, P.-R., and Raychaudhuri, S. (2019). Fast, sensitive and accurate integration of single-cell data with Harmony. Nat. Methods *16*, 1289–1296. https://doi.org/10.1038/s41592-019-0619-0.

118. Jin, S., Plikus, M.V., and Nie, Q. (2025). CellChat for systematic analysis of cell–cell communication from single-cell transcriptomics. Nat. Protoc. *20*, 180–219. https://doi.org/10.1038/s41596-024-01045-4.

119. Huang, B., Wang, B., Yuk-Wai Lee, W., Pong U, K., Leung, K.T., Li, X., Liu, Z., Chen, R., Lin, J.C., Tsang, L.L., et al. (2019). KDM3A and KDM4C regulate mesenchymal stromal cell senescence and bone aging via condensin-mediated heterochromatin reorganization. Iscience *21*, 375–390. https://doi.org/10.1016/j.isci.2019.10.041.

STAR★METHODS

KEY RESOURCES TABLE

REAGENT or RESOURCE	SOURCE	IDENTIFIER
Antibodies		
Rabbit Polyclonal anti-SIX2	Proteintech	Cat# 11562-1-AP; RRID: AB_2189084
Mouse Monoclonal anti-SIX2	Sigma Aldrich	Cat# SAB1401533; RRID: AB_10611294
Rabbit Polyclonal anti-PAX2	BioLegend	Cat# 901001; RRID: AB_2734656
Rabbit Monoclonal anti-WT1	Abcam	Cat# ab89901; RRID: AB_2043201
Mouse Monoclonal anti-SALL1	R&D Systems	Cat# PP-K9814-00; RRID: AB_2183228
Rat Monoclonal anti-PODXL (mouse)	R&D Systems	Cat# MAB1556; RRID: AB_2166010
Mouse Monoclonal anti-PODXL (human)	R&D Systems	Cat# MAB1658; RRID: AB_2165984
Sheep polyclonal anti-NPHS1	R&D Systems	Cat# AF4269; RRID: AB_2154851
Rabbit polyclonal anti-NPHS2	Abcam	Cat# ab50339; RRID: AB_882097
Biotinylated Lotus Tetragonolobus Lectin (LTL)	Vector laboratories	Cat# B-1325; RRID: AB_2336558
Rabbit Monoclonal anti-CDH1	Cell Signaling Technology	Cat# 3195; RRID: AB_2291471
Mouse Monoclonal anti-CDH1	BD Biosciences	Cat# 610182; RRID: AB_397581
Mouse Monoclonal anti-AQP1 (mouse)	Santa Cruz Biotechnology	Cat# sc-25287; RRID: AB_626694
Rabbit Monoclonal anti-AQP1 (human)	Abcam	Cat# ab168387; RRID: AB_2810992
Mouse Monoclonal anti-HNF4	R&D Systems	Cat# MAB4605; RRID: AB_3076456
Mouse Monoclonal anti-UPIIIb-C358	Provided from Xue-Ru Wu lab in NYU	N/A
Mouse Monoclonal anti-alpha-SMA (ACTA2)-Cy3	Sigma-Aldrich	Cat# C6198; RRID: AB_476856
Mouse Monoclonal anti-alpha-SMA (ACTA2)	Sigma-Aldrich	Cat# A5228; RRID: AB_262054
Goat Polyclonal anti-PDGFRB	R&D Systems	Cat# AF385; RRID: AB_355339
Rabbit Monoclonal anti-PDGFRB	Abcam	Cat# ab32570; RRID: AB_777165
Goat Polyclonal anti-GATA3	R&D Systems	Cat# AF2605; RRID: AB_2108571
Mouse Monoclonal anti-LRP2 (Megalin)	MyBioSource	Cat# MBS690201; RRID: AB_3677304
Sheep Polyclonal anti-Mouse Uromodulin	R&D Systems	Cat# AF5157; RRID: AB_2212556
Goat Polyclonal anti-SLC12A1	Abcam	Cat# ab240542; RRID: AB_2910116
Mouse Monoclonal anti-MEIS1/2/3	Active Motif	Cat# 39795; RRID: AB_2750570
Mouse Monoclonal anti-LIV2	MBL International	Cat# D118-3; RRID: AB_593027
Rabbit polyclonal anti-POU3F3	Thermo Scientific	Cat# PA5-64311; RRID: AB_2645790
Rabbit Monoclonal anti-ATP6V1B1	Abcam	Cat# ab192612; RRID: AB_2810993
Goat Polyclonal anti-FOXI1	Novus Biologicals	Cat# NB300-926; RRID: AB_10001201
Rabbit Monoclonal anti-RET (mouse)	Cell Signaling Technology	Cat# 3223; RRID: AB_2238465
Goat polyclonal anti-RET (human)	R&D Systems	Cat# AF1485; RRID: AB_354820
Rabbit Monoclonal anti-SOX9	Abcam	Cat# ab185230; RRID: AB_2715497
Rat Monoclonal anti-KRT8	DSHB	Cat# TROMA-I; RRID: AB_531826
Goat polyclonal anti-JAG1	R&D Systems	Cat# AF599; RRID: AB_2128257
Mouse Monoclonal anti-AQP2	Santa Cruz Biotechnology	Cat# sc-515770; RRID: AB_2810957
Rabbit polyclonal anti-AQP2	Alomone Labs	Cat# AQP-002; RRID: AB_2039728
Goat Polyclonal anti-FOXD1	Abcam	Cat# ab129324; RRID: AB_11150609
Rabbit Monoclonal anti-Renin	Abcam	Cat# ab212197; RRID: AB_2909418
Mouse Monoclonal anti-Epo (B-4)	Santa Cruz Biotechnology	Cat# sc-5290; RRID: AB_627551
Mouse Monoclonal anti-acetyl-alpha tubulin	EMD Millipore	Cat# MABT868; RRID: AB_2819178
Mouse Monoclonal anti-COL1A1	Proteintech	Cat# 67288-1-Ig; RRID: AB_2882554
Rabbit polyclonal anti-Fibronectin	Sigma-Aldrich	Cat# F3648; RRID: AB_476976
Goat Polyclonal anti-CD45	R&D Systems	Cat# AF114; RRID: AB_442146

(*Continued on next page*)

Continued

REAGENT or RESOURCE	SOURCE	IDENTIFIER
Rat Monoclonal anti-F4/80	Thermo Fisher Scientific	Cat# 14-4801; RRID: AB_2314387
Sheep Polyclonal anti-Human CD31	R&D Systems	Cat# AF806; RRID: AB_355617
Rat Monoclonal anti-Mouse CD31	BD Biosciences	Cat# 550274; RRID: AB_393571
Mouse Monoclonal anti-Human Nuclei	Sigma-Aldrich	Cat# MAB1281; RRID: AB_94090
Rabbit polyclonal anti- ENaC beta	StressMarq Biosciences	Cat# SPC-404; RRID: AB_10644173
Mouse Monoclonal anti-PCNA	Innovative Research	Cat# 18-0110; RRID: AB_86659
Mouse Monoclonal anti-ZO-1	Thermo Fisher Scientific	Cat# 33-9100; RRID: AB_2533147
Mouse Monoclonal anti-Desmin	Dako	Cat# M0760; RRID: AB_2335684
Goat Polyclonal anti-ITGA8	R&D Systems	Cat# AF4076; RRID: AB_2296280
Mouse Monoclonal PE anti-c-kit	BioLegend	Cat# 313204; RRID: AB_314983
DAPI	Thermo Fisher Scientific	Cat# D1306; RRID: AB_2629482
Chemicals, peptides, and recombinant proteins		
TTNPB	Cayman Chemical	Cat# 16144
FGF9	R&D Systems	Cat# 273-F9-025
Y-27632	Selleck Chemicals	Cat# S1049
Forskolin	Sigma-Aldrich	Cat# F3917-10MG
Aldosterone	Sigma-Aldrich	Cat# A9477
Vasopressin	Sigma-Aldrich	Cat# V0377-100IU
[deamino-Cys1, D-Arg8]-Vasopressin acetate salt hydrate (dDAVP)	Sigma-Aldrich	Cat# V1005-.1MG
[Arg8]-Vasopressin acetate salt	Sigma-Aldrich	Cat# V9879-1MG
(±)-Epinephrine	Cayman Chemical	Cat# 21245
3,3',5-Triiodo-L-thyronine	Cayman Chemical	Cat# 30996
Hydrocortisone 21-hemisuccinate (sodium salt)	Cayman Chemical	Cat# 18226
Dexamethasone	Cayman Chemical	Cat# 11015
25-hydroxy Vitamin D_3	Cayman Chemical	Cat# 9000683-1MG
Parathyroid hormone (1-34)	ApexBio	Cat# A1129-5MG
(Z)-4-Hydroxytamoxifen (4-OH-tamoxifen)	Sigma-Aldrich	Cat# H7904-5MG
Ethanol (control vehicle for 4-OH-tamoxifen treatment)	VWR	Cat# BDH1156-4LP
Lucifer Yellow-labeled dextran (10,000 MW)	Thermo Fisher Scientific	Cat# D-1825
Alexa Fluor 680-conjugated albumin	Thermo Fisher Scientific	Cat# A34787
Fluorescein Methotrexate	Thermo Fisher Scientific	Cat# M1198MP
6-CF (6-Carboxyfluorescein)	Thermo Fisher Scientific	Cat# C1360
BOCILLIN FL Penicillin	Thermo Fisher Scientific	Cat# B13233
TRITC-albumin	Sigma-Aldrich	Cat# A2289-10MG
Probenecid	Cayman Chemical	Cat# 1498-5MG
Cimetidine	Cayman Chemical	Cat# 18743
A83-01	Cayman Chemical	Cat# 9001799
Critical commercial assays		
TRIzol Reagent	Thermo Fisher Scientific	Cat# 15596026
Direct-zol RNA MicroPrep Kit	Zymo Research	Cat# R2062
DNA/RNA Shield	Zymo Research	Cat# R1100-50
Quick-RNA Microprep Kit	Zymo Research	Cat# R1051
iScript Reverse Transcription Supermix	Bio-Rad	Cat# 1708841
Ssoadvanced™ Universal SYBR	Bio-Rad	Cat# 1725274
AzuraView GreenFast qPCR Blue Mix LR	Azura Genomics	Cat# AZ-2320
QuantiChrom™ Urea Assay Kit	BioAssay Systems	Cat# DIUR-100
QuantiChrom™ Creatinine Assay Kit	BioAssay Systems	Cat# DICT-500

(*Continued on next page*)

Continued

REAGENT or RESOURCE	SOURCE	IDENTIFIER
RNAscope™ Multiplex Fluorescent Reagent Kit v2	Advanced Cell Diagnostics, Inc.	Cat# 323100
10x Genomics Chromium Single Cell 3'	10X Genomics	Cat# PN-1000075
GEM, Library & Gel Bead Kit	10X Genomics	Cat# PN-1000153
Chromium Single Cell B Chip Kit	10X Genomics	Cat# PN-1000282
10X Chromium Next GEM Single Cell Multiome ATAC + Gene Expression Reagent Kits	10X Genomics	Cat# PN-2000264
Click-iT™ Plus TUNEL Assay for In Situ Apoptosis Detection, Alexa Fluor™ 488 dye	Thermo Fisher Scientific	Cat# C10617
Deposited data		
Bulk RNA-seq of mouse kidneys, mouse kidney explants and mouse synthetic kidney organoids	This study	GSE264516
Single Cell Multiome of Day 24 mouse synthetic kidney organoids	This study	GSE262382
Single Cell Multiome of Day 25 human synthetic kidney organoids	This study	GSE272707
Single Nucleus RNA Sequencing (snRNA-Seq) of Day 5 human synthetic kidney organoids cultured with Stage I medium and TTNPB removal medium	This study	GSE297771
Single Nucleus RNA Sequencing (snRNA-Seq) of human synthetic kidney organoids transplants	This study	GSE297772
Single Cell RNA Sequencing (scRNA-Seq) of day 32 human kidney organoid transplants	Subramanian et al.[17]	GSE136314
Single Cell RNA Sequencing (scRNA-Seq) of 17-week human fetal kidneys	Kim et al.[47]	GSE232479
Single Nucleus RNA Sequencing (snRNA-Seq) of healthy adult kidneys and ADPKD patient kidneys	Muto et al.[85]	GSE185948
Additional supplemental figures deposited at Mendeley Data	This study	http://doi.org/10.17632/vs49gkxx95.1
Experimental models: Cell lines		
SIX2-GFP H1 hESC	Huang et al.[11]	N/A
SIX2-GFP/PAX2-RFP H1 hESC	Huang et al.[11]	N/A
SIX2-GFP/*PKD2*$^{-/-}$ #11 H1 hESC	Huang et al.[11]	N/A
WNT11-GFP/PAX2-RFP H1 hESC	Zeng et al.[14]	N/A
WTC11 iPSC	From Dr. Charles Murry's lab at USC (original cell line from UCSF)	N/A
CIRC2 iPSC	From Dr. Laura Perin's lab at CHLA	N/A
Experimental models: Organisms/strains		
Swiss Webster mice	Taconic Biosciences	Model # SW-F
NOD.Cg-*Prkdc*^{scid} *Il2rg*^{tm1Wjl}/SzJ NSG™ mice	The Jackson Laboratory	JAX # 005557; RRID:BCBC_4142
Six2$^{tm3(EGFP/cre/ERT2)Amc}$ mice (*Six2*^{GCE})	The Jackson Laboratory	JAX # 009600; RRID: IMSR_JAX:009600
Tg(Hoxb7-Venus)17Cos* mice	The Jackson Laboratory	JAX # 016252; RRID: IMSR_JAX:016252
Gt(ROSA)26Sor$^{tm1.1(CAG-cas9*,-EGFP)Fezh}$ mice	The Jackson Laboratory	JAX # 026179; RRID: IMSR_JAX:026179
Gt(ROSA)26Sor$^{tm14(CAG-tdTomato)Hze}$ mice	The Jackson Laboratory	JAX # 007908; RRID: IMSR_JAX:007908
Oligonucleotides		
See Methods S5		N/A
Software and algorithms		
ImageJ (version: 2.1.0)	Schneider et al.[109]	https://imagej.nih.gov/ij/; RRID: SCR_003070

(*Continued on next page*)

Continued

REAGENT or RESOURCE	SOURCE	IDENTIFIER
GraphPad Prism software (version: 9.1.0)	GraphPad Prism	GraphPad Prism (https://graphpad.com); RRID: SCR_015807
FlowJo software (version: 10.0.0)	FlowJo	FlowJo (https://www.flowjo.com/); RRID: SCR_008520
Partek Flow Genomic Analysis software	Partek Genomics Suite	Partek Genomics Suite (http://www.partek.com); RRID: SCR_011860
RStudio software	RStudio	RStudio (https://posit.co/); RRID: SCR_000432
CellChat	SciCrunch Registry	CellChat (https://github.com/sqjin/CellChat); RRID: SCR_021946
Metascape	SciCrunch Registry	Metascape (https://metascape.org); RRID: SCR_016620
ZEN Digital Imaging for Light Microscopy	ZEISS	ZEN Digital Imaging for Light Microscopy (http://www.zeiss.com/microscopy/us/products/software/zeiss-zen.html); RRID: SCR_013672
Olympus Cellsens Standard software	Olympus	Olympus cellSens Software (http://www.olympus-lifescience.com/en/software/cellsens); RRID: SCR_014551
Other		
Igfbp6	Advanced Cell Diagnostics, Inc.	425721-C1
Alx1	Advanced Cell Diagnostics, Inc.	403161-C3
Penk	Advanced Cell Diagnostics, Inc.	318761-C3

EXPERIMENTAL MODEL AND STUDY PARTICIPANT DETAILS

Human tissues

17-week human fetal kidney samples used in this study were collected under Institutional Review Board approval from University of Southern California. Following the patient decision for pregnancy termination, the patient was offered the option of donation of the products of conception for research purposes, and those that agreed signed an informed consent. This did not alter the choice of termination procedure, and the products of conception from those that declined participation were disposed of in a standard fashion. The only information collected was gestational age and whether there were any known genetic or structural abnormalities.

Mice

All experiments on animals were performed in accordance with institutional guidelines and IACUC protocol (USC IACUC Protocol # 20829) approved by University of Southern California. 6-8 weeks old female Swiss Webster mice were purchased from Taconic Biosciences (Model # SW-F). 6-8 weeks old NSG^{TM} mice (NOD.Cg-*Prkdc*^{scid} *Il2rg*^{tm1Wjl}/SzJ, JAX # 005557) were purchased from The Jackson Laboratory. 2-8 months old male *Six2*$^{tm3(EGFP/cre/ERT2)Amc}$ mice (*Six2*^{GCE}, JAX # 009600), *Gt(ROSA)26Sor*$^{tm1.1(CAG-cas9*,-EGFP)Fezh}$ mice (JAX # 026179) and *Tg(*Hoxb7-Venus*)17Cos* mice (JAX # 016252) were from Dr. Andrew McMahon, and used for mating with 6-8 weeks old female Swiss Webster mice. 6-8 weeks old male and female *Gt(ROSA)26Sor*$^{tm14(CAG-tdTomato)Hze}$ mice (tdTomato reporter mice, JAX # 007908) were from Dr. Kenneth Hallows. *Six2-tdTomato* (*Six2*-tdT) mice were generated through crossing 2-8 months old male *Six2*^{GCE} mice and 6-8 weeks old female tdTomato reporter mice. *Six2*-tdTomato (*Six2*-tdT)/*Hoxb7*-Venus mice were generated through crossing 2-8 months old male *Six2*-tdT mice with 6-8 weeks old female *Hoxb7*-Venus mice. All the mice were maintained on a 12 hours: 12 hours light-dark cycle with food and water ad libitum.

hPSC lines

Experiments using human pluripotent stem cells (hPSCs) were approved by the Stem Cell Oversight Committee (SCRO) of University of Southern California under protocol # 2018-2. Human pluripotent stem cells are routinely cultured in mTeSR1 Plus (STEMCELL Technologies #100-0276) medium in monolayer culture format coated with Matrigel (R&D Systems, # 3433-010-01) using Versene Solution (Thermo Fisher # 15040066) following the manufacturers' protocols.

METHOD DETAILS

Optimization of mouse kidney explant culture conditions to identify v2 medium

During kidney organogenesis *in vivo*, continuous nephron induction along with UB branching is achieved within the nephrogenic niche near the surface of the cortex of developing mammalian kidneys, which contains spatially organized kidney progenitor cells that continuously self-renew and differentiate to generate mature kidney cell types.[23,24] As first demonstrated by Grobstein in 1953,[110] explants of early mouse kidneys (E11.5-E12.5) cultured at an air-liquid interface in basal medium supplemented with 10% fetal bovine serum (FBS) undergo a developmental process mirroring *in vivo* development[42] (Mendeley Data Figure S1A). However, after reaching a developmental stage equivalent to an E15.5 kidney, kidney explants regress and lose their structural integrity.

We have previously shown that APEL2 basal medium supplemented with 0.1 μM TTNPB, a retinoic acid agonist (APEL2+TT, or "v0 medium"), can support the initial interactions between cultured mouse NPCs and UPCs *in vitro*.[11,14] Mouse kidney explants cultured in v0 medium exhibited significant branching morphogenesis of the *Hoxb7*-Venus$^+$ UB,[45] and formed early nephron structures that were stable for two weeks in culture (Mendeley Data Figure S1B). In contrast, switching the basal medium from APEL2 to a few other commercially available basal medium failed to support kidney explant growth and morphogenesis (Methods S1). However, under v0 medium culture, the tips of the elongated UB/CD started to regress around day 11 (Mendeley Data Figures S1B and S1H). Screening additional developmental signals and two common kidney hormones (vasopressin and aldosterone) (Methods S1) further identified FGF9, vasopressin, aldosterone, and TTNPB together (v1 medium), can double branching growth of the UPC derived collecting system, but tips still regressed starting around day 13 of culture (Mendeley Data Figures S1C, S1D, and S1H). Additional screening of physiologically relevant kidney hormones and small molecule agonists (Methods S1) identified a v2 medium supplemented with dDAVP (a vasopressin analog), epinephrine, and forskolin in which elongated UB/CD structures were retained for at least 3 weeks with no observed regression (Figures S1A and S1B; Mendeley Data Figures S1E–S1I; Methods S3; Video S1).

Analysis of progenitor populations in v2 medium cultured mouse kidney explants showed nephrogenic niche maintenance in which SIX2$^+$ NPCs cap KRT8$^+$/RET$^+$ UPCs (Figures S1C and S1D) and FOXD1$^+$ IPCs wrap around SIX2$^+$ NPCs (Mendeley Data Figures S2A and S2B). The nephrogenic niche number continues to grow as UB forms more branches from D3 to D7 (Figures S1C, S1D, and S1F; Mendeley Data Figures S2A–S2C and S2E), but declines around D13, and is exhausted by D15 (Figures S1E and S1F; Mendeley Data Figures S2C and S2E). From D7-D13, undifferentiated NPCs were maintained around UB branch tips, while induced NPCs started to generate nephrons that were fused with the branching UB network (Figure S1G; Mendeley Data Figures S2D–S2F). By D19-D21, *ex vivo* cultured kidneys are spatially organized along a radial axis resembling normal kidney assembly (Figures S1A and S1B). Segmented nephrons consist of WT1$^+$/PODXL$^+$ glomerulus-like structures (note these are not vascularized) (Figures S1H, S1K, and S4G), HNF4A$^+$/LRP2$^+$ proximal tubule (PT) (Figures S1H and S1I), AQP1$^+$ descending limb of loop of Henle (dLOH), SLC12A1$^+$/UMOD$^+$ ascending limb of loop of Henle (aLOH) (Figures S1I and S1J), and GATA3$^+$CDH1$^+$*Hoxb7*-Venus$^-$ distal nephron that is connected to GATA3$^+$CDH1$^+$*Hoxb7*-Venus$^+$ CD (Figure S1L). CDs form both KRT8$^+$/AQP2$^+$/SCNN1B(β-ENaC)$^+$ principal cell (PC) and FOXI1$^+$/ATP6V1B1$^+$ intercalated cell (IC) (Mendeley Data Figures S2H–S2J). Desmin+ mouse mesangial cells were identified in the glomerulus-like structures (Mendeley Data Figure S2K). MEIS1/2/3$^+$/PDGFRB$^+$ interstitial cells surround the nephrons and the CD (Figure S1K), and a PDGFRB$^+$/LIV2$^+$ renal capsule population forms the periphery of the structure (Mendeley Data Figure S2L). Primary cilia are found on the lumen side of the renal tubules, suggesting proper epithelial polarization (Mendeley Data Figure S2M). Periodic ureter peristalsis highlighted formation of ACTA2$^+$/AQP1$^+$ smooth muscle around the ureter (Figures S1J, S1M, and S1N; Video S2), which was observed from D7, peaking at D9-11, with an average interval of 12-15 seconds (Figure S1O).

Bulk RNA-seq profiling of time-course explant kidney development *ex vivo* confirmed the capture of key molecular events of nephrogenesis from NPC to different segments of the nephron (Figure S1P; Table S1), from UPC to CD (Figure S1Q; Table S1), and from IPC to stromal populations (Mendeley Data Figure S2N; Table S1). Principal component analysis (PCA) compared kidneys developing in vivo and confirmed stepwise *in vitro* maturation of kidney explants to kidneys resembling an early postnatal stage (Mendeley Data Figure S2O) contrasting to development observed in traditional *ex vivo* culture with 10% FBS (Figure S1R). These data collectively indicate the formation and spatial organization of major kidney nephron, CD, and stromal cell types in the *ex vivo* cultured kidney explant (Figure S1S). The optimized v2 medium from explant kidney culture was also used to support mSKO development.

Further development from v2 medium to v3 medium for hKPA culture

Small changes to the v2 medium, with shortened FGF9 treat time and the supplement of hormone hydrocortisone 21-hemisuccinate (HCHS) and A83-01, led to the development of v3 medium that supported hKPA development *in vitro* in this study. Shortened FGF9 was essential for continued spatial patterning of human nephron beyond the RV stage while HCHS and A83-01 kept hKPA healthy for a longer period than without it.

E12.5 mouse kidney *ex vivo* culture

Mouse E12.5 kidneys with intact ureter structure were dissected out from timed pregnant embryos and transferred onto 6-well format Transwell (Corning, Cat. No. 3450) for *ex vivo* culture. For culture with the traditional "10% FBS medium", 1mL 10% FBS medium was added in the bottom chamber (Day 0), and medium was changed every other day with fresh 10% FBS medium, with kidney explants harvested on Day 7. For culture with the "v0 medium", 1mL "v0 medium" (APEL2 + TTNPB) was added in the bottom chamber (Day 0), and medium was changed every other day, with kidney explants harvested on Day 17. For culture with the "v1 medium", 1mL Stage I medium was added in the bottom chamber (Day 0). On day 7, it was replaced with 1mL Stage II medium. On day 13, it

was replaced with 1mL Stage III medium. During each stage, the medium was changed every other day with their respective stage-specific medium. Kidney explants were harvested on day 19∼21 for various assays. For culture in the ''v2 medium'', 1mL Stage I medium was added in the bottom chamber (Day 0). On day 7, it was replaced with 1mL Stage II medium. On day 13, it was replaced with 1mL Stage III medium. On day 15, it was replaced with 1mL Stage IV medium. On day 17, it was replaced with 1mL Stage V medium. During each stage, medium was changed every other day with respective stage-specific medium. Kidney explants were harvested on day 19∼21 for various assays. Detailed culture medium components can be found in Methods S3.

Screening of additional factors supplemented into the "v2 medium"

Based on the ''v1 medium'', Stage III medium (APEL2/FGF9/aldosterone/vasopressin) was supplemented with dDAVP, dexamethasone, epinephrine, hydrocortisone 21-hemisuccinate, 3,3',5-Triiodo-L-thyronine or forskolin on day 13. Medium was changed every other day until kidney explants were harvested on day 19 for various assays.

Mouse NPC and UPC expansion

Mouse NPC lines were derived and maintained for long-term culture with mNPSR-v2 following our previously described protocol.[11] Mouse UPCs (UB organoids) were expanded with mUBCM (mouse), following our previously described protocol.[14] Recipes of mNPSR-v2 and mUBCM media can be found in Methods S2.

Generation of mKPA from expandable mouse NPCs and UPCs

Mouse NPCs were dissociated into single cells with Accumax Cell Dissociation Solution (Innovative Cell Technologies, Cat. No. AM105) following our previously described protocol.10 Cell number was counted with TC20™ Automated Cell Counter (Bio-Rad, Cat. No. 1450102). 5-10 mouse UB organoids (UPCs) were pooled together into a 1.5mL Eppendorf tube. After removing the culture medium from the tube, 1mL cold Cell Recovery Solution (Corning, Cat # 47743-696) was added to the tube and rock-incubated for 1 hour at 4°C to dissolve the Matrigel. After the 1-hour rock-incubation, all Matrigel was dissolved and all the mouse UB organoids were at the bottom of the tube. Cell Recovery Solution was then removed and mouse UB organoids were washed once with 1mL 1x PBS. Next, 500μL prewarmed Accumax was added into the tube fast enough to resuspend the organoids without further pipetting. The tube was then incubated in a 37°C incubator for 8 minutes, with a gentle tap to resuspend the organoids at 4 minutes. Timing was critical as we were aiming for incomplete dissociation, with around 50%-60% single cells and 40%-50% small clusters with 10-30 cells. During this process, we ensured all the organoids were settled at the bottom of the tube to ensure thorough dissociation. After 8 minutes of incubation, 500μl hBI medium (see Methods S2 for medium recipe) was used to neutralize the Accumax. Gently pipette 6-7 times to break up the 3D UB organoid structures. The tube was then centrifuged at 300g for 5 minutes, then aspirated the supernatant, and resuspended the cell pellet with Stage I medium. Typically, 1/3 of a fully-grown day 5 mouse UB organoid, or approximate 30,000 UB cells, was combined with 45,000 mouse NPCs to generate one mouse kidney progenitor assembloid (mKPA) aggregate (Note: Based on our experiences, cell counting with TC20™ Automated Cell Counter (Bio-Rad, Cat. No. 1450102) was usually not accurate for this type of sample, in which small clusters of cells remain. It would calculate 30,000 cells to be around 15,000 cells. So, we typically rely on the 1/3 ratio to determine the amount of UB cells to incorporate into the mKPA aggregate). Dissociated NPC single cells and incompletely dissociated mUB cells were combined in a 1.5mL Eppendorf tube, centrifuged at 300g for 5min, then resuspended with Stage I medium + Y-27632_10μM (use 100μL per mSKO aggregate). For each mKPA aggregate generated, 100μL resuspended cell solution was transferred into each well of a U-bottom 96-well plate (Thermo Fisher Scientific, Cat. No. 174929), centrifuged at 300g for 5 minutes, and cultured in 37°C incubator overnight for aggregation. The following day (Day 0), mKPA aggregates were transferred onto 6-well format Transwell (Corning, Cat. No. 3450) with 1mL Stage I medium in the bottom chamber. On day 7, the current Stage I medium was removed and replaced with 1mL Stage II medium. On day 13, the medium was switched to 1mL Stage III medium. On day 15, it was switched to 1mL Stage IV medium. On day 17∼22, then switched to 1mL Stage V medium. During each stage, 1mL medium in the bottom chamber was changed every other day with corresponding stage-specific medium. mKPA were harvested on day 19∼24 for various assays. Detailed recipe of the medium components can be found in Methods S3.

Functional assays to assess various tubular and endocrine functions *in vitro*

Dextran uptake assay

3-4x D22 mKPA were transferred to one well of a 24-well plate, followed by incubation with 100 mg/mL of fluorescence-labeled dextran for 4 hours (pulse) in 1mL Stage IV medium under shaking culture condition (Shaking at 120 rpm). 4 hours later, remove the medium and wash mKPA 3 times with PBS, and then transfer the mKPA onto Transwell membrane with 1mL fresh Stage IV medium in the bottom well, they were ready for imaging. Live cell imaging was conducted utilizing IX73 Inverted Microscope (pulse). mKPA were then cultured without dextran for another 24 hours (chase), before being fixed for immunofluorescence analysis.

TRITC-albumin (Albumin, Tetramethylrhodamine) uptake assay

4x D22 mKPAs or 4x D21 hKPAs were transferred to one well of a 24-well plate from Transwell membrane and followed by incubation with 10μg/mL of TRITC-albumin for overnight in 1mL Stage IV medium under shaking culture condition (Shaking at 120 rpm). After incubation overnight, remove the culture medium and wash KPAs 3 times with PBS, and then transfer these KPAs onto Transwell membrane with 1mL fresh Stage IV medium in the bottom chamber, they were ready for imaging. Live cell imaging was captured utilizing IX73 Inverted Microscope. After live cell imaging, the KPAs were fixed for immunofluorescence analysis.

DAPI uptake assay

6-8x D22 mKPAs were transferred to two wells of a 24-well plate from Transwell membrane (3-4x KPA/group) and followed by incubation with 1.4μM DAPI or 1.4μM DAPI + 200μM cimetidine for 30 mins in 1mL Stage IV medium under shaking culture condition (Shaking at 120 rpm). 30 mins later, remove the culture medium and wash KPAs 3 times with PBS, and then transfer these KPAs onto Transwell membrane with 1mL fresh Stage IV medium in the bottom chamber, they were ready for imaging. Live cell imaging was captured using IX73 Inverted Microscope. After live imaging, these KPAs were fixed for immunofluorescence analysis.

6-CF (6-Carboxyfluorescein) uptake assay

6-8x D22 mKPAs were transferred to two wells of a 24-well plate from Transwell membrane (3-4x KPAs/group) and followed by incubation with 1μM 6-CF or 1μM 6-CF + 2.5mM probenecid for 1 hour in 1mL Stage IV medium under shaking culture condition (Shaking at 120 rpm). 1 hour later, remove the medium and wash KPAs 3 times with PBS, and then transfer the KPAs onto Transwell membrane with 1mL fresh Stage IV medium in the bottom chamber, they were ready for imaging. Live cell imaging was captured using IX73 Inverted Microscope. After live cell imaging, the KPAs were fixed for immunofluorescence analysis.

Methotrexate uptake assay

3-4x D22 mKPAs were transferred to one well of a 24-well plate from Transwell membrane and followed by an incubation with 10μM of fluorescence-labeled methotrexate for 4 hours in 1mL Stage IV medium under shaking culture condition (Shaking at 120 rpm). 4 hours later, remove the medium and wash KPAs 3 times with PBS, and then transfer these KPAs onto Transwell membrane with 1mL fresh Stage IV medium in the bottom well, they were ready for imaging. Live cell imaging was conducted utilizing IX73 Inverted Microscope. After live cell imaging, the KPAs were fixed for immunofluorescence analysis.

BOCILLIN FL Penicillin uptake assay

3-4x D22 mSKOs or 3-4x D21 hKPAs were transferred to one well of a 24-well plate from Transwell membrane and followed by incubation with 10μM of BOCILLIN FL Penicillin for 30 mins or 4 hours in 1mL Stage IV medium under shaking culture condition (Shaking at 120 rpm). After 30 mins or 4 hours incubation, remove the medium and wash KPAS 3 times with PBS, and then transfer these KPAs onto Transwell membrane with 1mL fresh Stage IV medium in the bottom chamber, they were ready for imaging. Live cell culture images were captured using IX73 Inverted Microscope. After live cell imaging, these KPAs were fixed for immunofluorescence analysis.

Renin secretion assay

3-4x D19 mKPAs were treated with 10 μM forskolin or 0.1% DMSO for 1 day or 3 days, and then KPAs were harvested for RNA and fixed for immunofluorescence analysis.

Erythropoietin (EPO) secretion assay

3-4x D19 mKPAs were cultured under normoxia (20% O_2) or hypoxia (4% O_2) condition for 1 day or 2 days, and then KPAs were harvested for RT-qPCR and fixed for immunofluorescence analysis.

Treatment with 25(OH)D_3 (25-hydroxy Vitamin D_3) and PTH

4x D22 mKPAs were transferred to one well of a 24-well plate from Transwell membrane, and followed by incubation with 100nM or 500nM 25(OH)D_3, or 500nM 25(OH)D_3 + 10nM or 50nM parathyroid hormone (PTH), or 50nM PTH, or PBS (CTRL) for 24 hours in 1mL Stage IV medium under shaking culture condition (Shaking at 120 rpm). 24 hours later, KPAs were harvested for RT-qPCR.

Mouse Kidney Progenitor Assembloid transplantation into immunodeficient NSG mice

D3 mKPAs were collected for transplantation on mesentery site of NSG mice. Before transplantation, 5-10x D3 mSKOs were detached from Transwell membrane using 30G needle and transferred into 1.7mL tube containing 10% FBS medium. Briefly, D3 mKPAs generated with *Six2*-tdT mouse NPCs and wildtype D5 mouse UPCs (UB organoids) on Transwell membrane following protocols described above. 6-8 weeks old NSG™ mice (NOD.Cg-*Prkdc*^{scid} *Il2rg*^{tm1Wjl}/SzJ, JAX # 005557) were used for transplantation. Mesentery transplantation protocol (#20829) was approved by IACUC. All surgery procedures were performed under anesthesia using isoflurane and aseptic techniques. Buprenorphine-SR (0.5-1.0/kg, administrated subcutaneously) was given preemptively before making incision to prevent pain wind-up. Sterile surgical gloves were used. Instruments were sterilized utilizing the autoclave prior to surgery. Instruments were sterilized between animals using a hot-bead sterilizer during the surgery. The surgical site was shaved, and the skin was prepped with 3 alternating scrubs of betadine and 70% ethanol. A 2-3cm incision was made in the midline, and sterilized cotton swab and fine forceps were used to take the intestines out of the body and extend the mesentery. 4-5x D3 mKPAs were separately placed on the mesentery site. The transplanted mKPAs were immobilized with 100% MTG. After that, the abdominal wall and skin were closed individually. The abdominal wall was closed using absorbable sutures (PDS or Vicryl 5-0 or 6-0 size). Skin was closed by standard suturing techniques using synthetic non-absorbable sutures such as prolene for skin (5-0 or 6-0). After that, the mice were placed within a clean cage on a 37 °C warming tray during the surgery/recovery period (10-15 minutes). Animals were monitored continuously until full recovery from anesthesia. 14-27 days after transplantation, the surgical mice were euthanized, and the transplants were collected for various assays as described.

Human kidney progenitor assembloids transplantation into immunodeficient NSG mice

D5-D7 (RV-stage) hKPAs (wildtype and PKD2$^{-/-}$) were collected for transplantation under the renal capsule of NSG mice. Before transplantation, 5-10x D5-D7 hKPAs were detached from Transwell membrane using 30G needle and transferred into 1.7mL tube containing 10% FBS medium. 6-8 weeks old NSG™ mice (NOD.Cg-*Prkdc*^{scid} *Il2rg*^{tm1Wjl}/SzJ, JAX # 005557) were used for transplantation. Renal capsule transplantation protocol (#11893) was approved by IACUC. All surgery procedures were performed under

anesthesia using isoflurane and aseptic techniques. Buprenorphine-SR (0.5-1.0/kg, administrated subcutaneously) was given pre-emptively before making incision to prevent pain wind-up. Sterile surgical gloves were used. Instruments were autoclaved for sterilization prior to surgery. Instruments were sterilized between animals using a hot-bead sterilizer during the surgery. The surgical site was shaved, and the skin was prepped with 3 alternating scrubs of betadine and 70% ethanol. A 2-3cm incision was made in the back, and sterilized cotton swab and fine forceps were used to take the kidney out of the body. 21G needle was used to gently generate a small pore on renal capsule without significant bleeding. 20G Catheter (SurFlash® Polyurethane I.V. Catheters, Terumo®) was utilized to collect and transfer 5-10x hKPAs under renal capsule. After that, the muscle layer and skin were closed individually. The muscle layer was closed using absorbable sutures (PDS or Vicryl 5-0 or 6-0 size). Skin was closed using 7mm Reflex Clip Applier. After that, the mice were placed in a clean cage on a 37 °C warming tray during the surgery/recovery period (10-15 minutes). Animals were monitored continuously until full recovery from anesthesia. 14-70 days after transplantation, the surgical mice were euthanized, and the transplants were collected for various assays as described. In this study, D5-D7 wildtype hKPAs were transplanted into 17 NSG mice (n=17) and D5-D7 PKD2$^{-/-}$ hKPAs were transplanted into 7 NSG mice (n=7) with consistent phenotypes.

Intravital imaging using multiphoton microscopy (MPM)

Surgical implantation of a ventral abdominal imaging window (AIW) above the KPAs that were previously transplanted into the mesentery of 6-8 weeks-old NSG^{TM} mice (NOD.Cg-*Prkdc*^{scid} *Il2rg*^{tm1Wjl}/SzJ, JAX # 005557) was performed using aseptic surgical procedures under continuous anesthesia (Isoflurane 1-2% inhalant via nosecone using the SomnoSuite low-flow anesthesia system, Kent Scientific, Torrington, CT) as described recently.[111] Mice were placed on the stage of an inverted microscope with continuous isoflurane anesthesia and body temperature was maintained with a homeothermic blanket system (Harvard Apparatus) as described previously.[112] Alexa Fluor 680-conjugated albumin (ThermoFisher, Waltham, MA) was administered iv. by retro-orbital injection to label the circulating plasma (30 μL iv. bolus from 10 μg/ml stock solution). Single intravital MPM imaging sessions of the KPAs were performed through the AIW using a Leica SP8 DIVE multiphoton confocal fluorescence imaging system with a Leica 25x water immersion objective (numerical aperture (NA) 1.0) powered by a Chameleon Discovery laser at 960 nm excitation (Coherent, Santa Clara, CA) and a DMI8 inverted microscope's external Leica 4Tune spectral hybrid detectors (emission at 480 nm for second harmonic generation (SHG), 510–530 nm for lucifer yellow, 580–640 nm for tdTomato, and 680–740 for AF680, Leica Microsystems, Heidelberg, Germany).[112] The potential toxicity of laser excitation and fluorescence to the cells was minimized by using a low laser power and high scan speeds to keep total laser exposure as minimal as possible. Fluorescence images were collected in volume and time series (xyt, 526 ms per frame) with the Leica LAS X imaging software and using the same instrument settings (laser power, offset, gain of both detector channels). The strong, positive fluorescence signal from the genetic reporter tdTomato and RFP and high-resolution MPM imaging allowed for easy identification of KPAs structures and cells. Quantitative imaging of KPAs glomerular vascular permeability was performed by measuring the appearance of the systemically injected fluid marker Lucifer Yellow dye bolus (10 μl of a 10 mg/ml stock in iv bolus, Invitrogen) around glomerular capillaries as described previously.[113] Image analysis was performed using the Quantify package of LAS X software (3.6.0.20104; Leica-Microsystems).

Patch Clamp

Single-channel activity was recorded using the cell-attached patch-clamp configuration under voltage-clamp conditions, as previously described.[114] Briefly, potassium channel activity was measured from the basolateral side of the organoid's tubules, which displayed morphological characteristics resembling the proximal tubules (PT) under light microscopy. Recordings were obtained using an Axopatch 700B amplifier connected via a Digidata 1440A interface to a PC and analyzed with the pClamp 10.6 software suite (Molecular Devices; RRID: SCR_011323). Signals were low-pass filtered at 0.3 kHz using a Bessel filter (LPF-8, Warner Instruments). Current–voltage (I–V) relationships were determined by monitoring channel activity at pipette holding potentials ranging from –80 mV to +60 mV, in 20 mV increments. All experiments were conducted at room temperature (22–24 °C). Patch pipettes were pulled using a horizontal puller (P-97, Sutter Instruments) and had resistances between 9 and 14 MΩ when filled with pipette solution. The extracellular (bath) solution contained (in mM): 150 NaCl, 5 KCl, 1 $CaCl_2$, 2 $MgCl_2$, 5 glucose, and 10 HEPES (pH 7.35). The pipette (intracellular) solution contained (in mM): 150 KCl, 2 $MgCl_2$, and 10 HEPES (pH 7.35).

Quantification and identification of urea and creatinine in cyst fluid collected from mKPAs and hKPAs transplant

Cyst fluid was collected from mKPAs transplants (n=3) and PKD2$^{-/-}$ hKPAs transplants (n=3). Mouse serum and urine was collected from healthy 2-month-old adult mice (n=3). QuantiChrom^{TM} Urea Assay Kit and QuantiChrom^{TM} Creatinine Assay Kit were applied to identify and measure the concentration of urea and creatinine in KPAs transplant-collected cyst fluid, mouse serum and mouse urine.

iNPC and iUPC expansion

i. Generation and expansion of hESC-derived iNPC lines and iUPC lines. hESC-derived iNPC lines were generated following the protocols as described previously.[11] hESC-derived iNPCs were cultured with hNPSR-v2 medium. hESC-derived iUPC lines were generated following the protocols as described previously.[14] hESC-derived iUPCs were cultured with hUBCM-v2 medium.

ii. Generation and expansion of iPSC-derived iNPC lines and iUPC lines. WTC-11 iPSC line and CIRC-2 iPSC line were used to derive iNPC lines and iUPC lines following the protocols described previously.[11,14] Since iPSC lines do not have *SIX2*-GFP reporter, ITGA8 antibody (R&D Systems, Cat# AF4076) was used to enrich iNPCs after iPSC differentiation. c-Kit antibody (BioLegend, Cat# 313204) was used to enrich iUPC precursor cells after iPSC differentiation, as described previously.[14] Purified

iNPCs were further cultured with hNPSR-v2 medium to derive iNPC lines. Purified iUPC precursor cells were further cultured with hUBCM-v2 medium to derive iUPC lines. Before assembling hKPAs, iNPC lines and iUPC lines were characterized to verify NPC and UPC marker gene expression through immunofluorescence staining and RT-qPCR assays. Recipes of hNPSR-v2 and hUBCM-v2 media can be found in Methods S2.

Generation of human kidney progenitor assembloids from expandable iNPCs and iUPCs

Our previously described WNT11-GFP/PAX2-RFP and WTC11 iUPC line (iUB organoid), cultured in hUBCM-v2 medium, was utilized to assemble human kidney progenitor assembloid.[14] *WNT11*-GFP reporter was routinely used to assess the undifferentiated UPC identity. To dissociate the iUB organoids into single cells, the iUB organoids were collected and transferred to a 1.5 mL Eppendorf tube with 1 mL of Cell Recovery Solution (Corning, #354253), followed by a 1-hour shaking at 4°C to dissolve Matrigel. After the 1-hour incubation, the cell recovery solution was removed, and 500 μL of warmed-up Accumax was added and incubated for 10 minutes at 37°C. After the 10-min incubation, 500 μL of 10% FBS in DMEM was added, followed by gently pipetting up and down for 4-5 times to disrupt the iUB organoids into small clusters. The dissociated iUB cells were counted, and $1x10^4$ cells were seeded to each well of a 96-well U-bottom plate with 100μL of hUBCM-v2 medium[14] and 10 μM Y27632. The plate was then centrifuged at 300g for 5 minutes and then placed in the incubator where it won't be perturbed to allow the formation of iUB aggregate overnight for subsequent mixing with iNPCs (see below). Our previously described *SIX2*-GFP, SIX2-GFP/PAX2-RFP, *SIX2*-GFP/*PKD2*$^{-/-}$, WTC11 iNPC lines was utilized to assemble hKPAs.[11] The iNPCs were cultured in hNPSR-v2 medium with a monolayer culture system. The iNPCs used to assemble the hKPAs in this study were cultured in hNPSR-v2 medium up to 4 weeks post the initial FACS purification.

On day 0 of hKPAs formation, iNPCs at a confluency of >90%, were washed with PBS and dissociated to single cells with Accumax for 8 minutes. The Accumax activity was then quenched by adding 1:1 ratio of 10% FBS with DMEM. The dissociated iNPC single cells were counted and $5X10^4$ iNPCs were added to one well of a 96-well U-bottom plate in 100 μL of Stage I media (APEL™ 2 medium containing 10 ng/ml hFGF9 and 0.1μM TTNPB). 10 μM Y27632 was added overnight to increase the survival of the aggregation formation. After seeding the iNPCs, one iUPC aggregate described above was manually added to each well with minimal carry-over of hUBCM-v2. Once the iUPC aggregate was added to each well, it is then centrifuged at 300g for 5 min to ensure the iUPC aggregate was in the center. Carefully place the 96-well U-bottom plate back to the incubator where minimal perturbation would occur to allow the successful aggregation overnight. This was considered Day 0 of the hKPAs timeline.

After 24-hour incubation, a hKPAs aggregate in which the iNPCs form a sphere-like structure wrapping around the central iUPC aggregate was formed. It was then transferred to a 6-well format Transwell plate (Corning, Cat. No. 3450) for continued culture at the air-liquid interface. Before transferring the hKPA, add 1 mL of the Stage I medium to the bottom of the Transwell membrane. A P200 pipette, with the tip cut to allow a greater diameter, was used to transfer the hKPAs aggregate without disrupting its structural integrity. 6 aggregates were typically put onto each Transwell to allow enough room for hKPAs growth. Remove any residual medium that was carried over during the transfer with a P20 or P200 pipette. This ensures the hKPAs to stick to the Transwell membrane. The hKPAs was cultured in Stage I medium from Day 0-7, Stage II medium from Day 7-15, Stage III medium from Day 15-21, Stage IV medium from Day 21-22, and Stage V medium from D22 onwards, with the medium being renewed every other day. The hKPAs was harvested at different time points as described for various assays. Schematic of the protocol overview can be found in Figure S7A and stage-specific medium composition can be found in Methods S3. For the +/- TTNPB experiment, the +TTNPB group followed the standard protocol as described above, but TTNPB was removed from for the -TTNPB group. The hKPAs were harvested at D6 for snRNA-seq analysis and immunofluorescence staining analysis, and at D25 for end-point immunofluorescence staining analysis.

Note that, based on our experiences working with different hPSC lines, adjustment of stage-specific medium duration of the protocol is necessary. The timing is based on morphological changes under bright-field microscope. In particular, switching to stage III medium can range from D14-D15 when clear head-tail nephron structures have established. hKPAs can be harvested for various assays as early as 2 days after FSK treatment and as late as D30 in our hands across different hPSC lines.

We use two main criteria to assess successful hKPA assembly: (1) the formation of polarized RV structures surrounding the central UB in early-stage hKPAs, and (2) the formation of segmented nephrons fused to the central collecting duct CD at the endpoint of hKPA development. Depending on the iNPC/iUPC lines and experimental batch, the success rate—defined as the percentage of organoids meeting both criteria—ranges from 75% to 100%. Variability in self-organization during aggregation, particularly the positioning of the iUPC aggregate relative to the surrounding iNPCs, can impact development. For instance, if the iUPC aggregate is not centrally located, hKPA formation may fail or induce fewer RVs. Additionally, we observe variability in both the number of RVs formed and the number of nephron–CD connections, across and within experimental batches.

Bulk RNA sequencing

Kidney Progenitor Assembloids, *ex vivo* cultured kidney explants, and mouse kidneys at different developmental stages from E12.5 to postnatal day 45 (P45), were collected and lysed in TRIzol reagent or DNA/RNA Shield and stored under -80°C. Total RNA was extracted using Direct-zol RNA MicroPrep Kit (Zymo) or Quick-RNA Microprep Kit (Zymo). Extracted RNA samples were sent to Novogene USA Inc. for bulk RNA-seq library preparation and sequencing.

Bulk RNA-seq data analysis

RNA sequencing data was analyzed using Partek Flow Genomic Analysis Software. FASTQ files were trimmed from both ends based on a minimum read length of 25 bps and an end minimum quality score (Phred) of 20 or higher. Reads were aligned to mm39 using STAR 2.7.8a. Aligned reads were quantified to the Partek E/M annotation model. Gene counts were normalized using DESeq2 Median ratio. Principal component analysis (PCA) for Figures 1R and 2N and Mendeley Data Figure S1L was performed using mouse kidney-associated signature genes (Table S1). Hierarchical clustering of selected genes was produced based on the genes' DESeq2 Median ratio values, clustering samples and features with average linkage cluster distance and Euclidean point distance. All processed bulk RNA-seq data are summarized in Table S1.

Single nuclei isolation from kidney progenitor assembloid

The mKPAs and hKPAs were harvested for 10x Genomics Multiome (snRNA/snATAC-seq) assays at Day 24 and 25 time point (*in vitro*), respectively. 10 mKPAs and 14 hKPAs were used for Multiome assay, in which every two KPAs were dissociated together in a 1.5mL Eppendorf tube. For *in vivo* experiments, wildtype hKPAs transplants (32 days and 59 days post transplantation) and PKD2$^{-/-}$ hKPAs transplants (66 days post transplantation) were dissected out from the host NSG mouse, with the mouse renal capsule carefully removed by manual microdissection. hKPAs transplants were then minced into small pieces using blade. mKPAs and hKPAs were dissociated using 10 mg/mL Bacillus licheniformis cold active protease (Sigma P5380) mixed with 10 mg/mL collagenase type 4 (Worthington, #LS004188) and 125 U/mL DNase I (Worthington, #LS002058) in DPBS at 12°C for 35 min (1 mL total reaction volume). The dissociation reaction mix was mixed twenty times with P200 pipette every 5 minutes. The dissociation reaction was terminated by adding 1 mL of 20% fetal bovine serum diluted in DPBS (final FBS concentration 10%). Cell viability was assessed (97%) following by adding 5 mL of AutoMACS (now total volume 7mL) and spinning down at 300g for 5 mins. The supernatant was removed as much as possible, and the cell pellets were resuspended with prechilled nuclear lysis buffer supplemented with RNase inhibitors as outlined in 10X protocol (CG000365 RevC). Nuclear lysis reaction was incubated on ice for 5 mins and then quenched with wash buffer and spun down at 500g for 5 min at 4°C. Cell viability dropped to 5% during this time. The nuclear pellet was washed and spun down twice filtered through 40μM filter (pluriSelect,43-50040), and pelleted at 500g for 5 minutes at 4°C in a swinging bucket centrifuge. The pellet was resuspended in prechilled diluted Nuclei Buffer (10X Genomics, #2000207) + RNase inhibitors. Then targeted number of nuclei were moved to transposition mix and proceeded to drop-seq separation on the 10X machine (Chip j) after 1 hour incubation.

snRNA-seq and snATAC-seq library construction and sequencing

Nuclei concentration was assessed and a target of ~13,000 x 2 nuclei (in two technical replicates) were loaded into two separate Tn5 transposition reactions. Loading onto Chip J, GEM Generation and Library Preparation followed the manufacturer's protocol (10X Genomics, CG000338) with 7 preAmp, 7 ATAC Library, 8 cDNA, and 14 SI GEX PCR cycles used. All cleanups were performed using suggested SPRI-Select bead ratios. Final library concentration and quality were assessed by BioAnalyzer. Complementary snRNA (GEX) and snATAC libraries were then sequenced on the Illumina-S4 Novaseq 6000 platform at Novogene.

Data analysis for snRNA-seq/snATAC-seq datasets

Preprocessing and quality-control

Raw sequencing data were preprocessed using Cell Ranger ARC (v.2.0.1) for multiome datasets and cellranger (v6.0.0) for standalone snRNA-seq data. Reference genomes (mouse mm10 and human hg38) were obtained from the 10x Genomics website and supplemented with custom tdTomato and Venus sequences to enable accurate alignment. The cellranger-arc count or cellranger count pipelines were used to generate feature-barcode matrices. These filtered matrices were imported into R and processed using the Seurat (Read10X_h5 or Read10X) and Signac packages (Seurat v5.0.3, Signac v1.11.0) to create Seurat objects containing RNA and ATAC modalities. Quality control (QC) was performed based on multiple metrics. Cells were excluded if they fell into the top or bottom 5% for any of the following: number of genes detected, total RNA UMIs, ATAC fragment counts, or nucleosome signal. Additional exclusion criteria included TSS enrichment in the bottom 5% and excessive mitochondrial content (thresholds: <40% for mouse, <20% for human). After applying quality-control metrics and eliminating potential sequencing artifacts using the Seurat V5 R package,[100] we retained the following high-quality nuclei:

mSKOs (n=4 biological replicates): 36,801 nuclei, median 2,421 genes/nucleus (snRNA-seq), and 13,116 fragments/nucleus (snATAC-seq).

hKPAs *in vitro* (n=2 replicates): 20,112 nuclei, median 2,124 genes/nucleus (snRNA-seq), and 14,760 fragments/nucleus (snATAC-seq).

hKPAs with or without TTNPB (n=2 replicates): 25,244 nuclei, median 5,778 genes/nucleus (snRNA-seq).

hKPAs *in vivo* (n=5 samples): 38,980 nuclei, median 1,496 genes/nucleus (snRNA-seq).

Sample integration and dimension reduction

RNA and ATAC assays were integrated separately. For RNA, samples were integrated into a unified scRNA-seq data object using CCA integration in Seurat. After removing low quality clustered cells, Non-linear dimension reduction was performed with RunUMAP and FindNeighbors functions using 30 principal components (PCs), followed by graph-based clustering. For ATAC, peaks in the datasets were intersected to obtain overlapping genomic regions, filtered, and merged. Normalization and linear dimension reduction were performed using latent semantic indexing (LSI) in Signac, followed by CCA integration and non-linear dimension

reduction with RunUMAP. Gene activity scores were calculated to assess chromatin accessibility associated with each gene, summing total ATAC fragments fall into gene bodies and 2kb upstream regions of transcription start site (TSS) according to the Bioconductor R package EnsDb.Mmusculus.v79(v.2.99.0) and EnsDb.Hsapiens.v86(v2.99.0).

Cell type annotation and subclustering analysis

Cell type annotation was primarily based on integrated RNA objects, with subclustering performed for specific cell populations. Annotations were validated using classical marker genes, and cell identities were assigned to corresponding ATAC objects. The reliability of annotations was confirmed by examining gene activity scores of marker genes. See also Table S2 for the top 200 differentially expressed gene (DEG) lists of different cell clusters from snRNA-seq.

Analysis of snRNA-seq and snATAC-seq data of P0 mouse kidneys, 17-week human kidneys, and Other Public Single Cell Datasets

P0 mouse kidney and 17-week human kidney datasets[47] were processed followed procedures similar to single-cell multiomics data, with separate approaches for snRNA-seq and snATAC-seq datasets. For snRNA-seq data, canonical correlation analysis (CCA) integration was performed using Seurat with default parameters, as described in the official Seurat vignette. For snATAC-seq data, gene activity scores were computed and used as input for CCA-based integration. To identify shared variable features, we selected the top 3,000 highly variable genes from the KPAs, P0 mouse kidney, and 17-week human kidney RNA datasets and used their union for downstream analysis.

Other publicly available single-cell datasets were analyzed using similar preprocessing, integration, and quality-control strategies.

Motif enrichment analysis

Cell type-specific motif enrichment was assessed by computing a per-cell accessibility score for established motifs within the accessible regions of each cell. This was achieved using the chromVAR(v.1.24.0) and chromVARmotifs(v.0.2.0) package with cisBP motif collections (“human_pwms_v2”) and the RunChromVAR function in Signac.

Visualization of single-cell data

Most plots were visualized by the Seurat or Signac plotting functions guided by the Seurat visualization vignettes, using DimPlot, DotPlot, FeaturePlot, CoveragePlot functions.

Assessment of Maturity in hKPAs

To evaluate the maturation state of hKPAs, we performed differential gene expression analysis using publicly available single-cell datasets from 17-week human fetal kidney (hFK)[47] and human adult kidney (hAK).[85] Differentially expressed genes (DEGs) were identified using the Wilcoxon rank-sum test implemented in Seurat’s FindMarkers function. Genes with an adjusted P-value < 0.01 were considered significant and were ranked by average log2 fold change.

For each cell type in the hAK dataset, the top 500 genes with the highest avg_log2FC were selected to form a reference gene set representing mature kidney cell signatures. Expression levels of these genes were then compared across corresponding cell types in hFK and hKPA samples to assess the degree of maturation.

Differential Expression and Gene Set Enrichment Analysis

Differentially expressed genes (DEGs) between experimental groups were identified using the Wilcoxon rank-sum test implemented in Seurat’s FindMarkers function. Genes with an adjusted P-value < 0.01 and an absolute log2 fold change (|avg_log2FC|) > 1 were considered significantly differentially expressed. Significantly altered genes were subsequently subjected to gene set enrichment analysis using the Metascape web platform (https://metascape.org).[115] To further explore underlying biological mechanisms, we additionally downloaded the Human MSigDB v2024.1.Hs release from the MSigDB database, which includes 34,837 individual gene sets and performed enrichment analysis using the clusterProfiler R package.[116]

Cross-Species Integration of Human and Mouse Cells

Gene symbols in the mouse dataset were converted to their human orthologs using the biomaRt R package.[98,99] The resulting “humanized” mouse expression matrix was merged with the human dataset using the merge function in Seurat v5. The combined Seurat object was normalized using SCTransform, followed by dimensionality reduction via PCA and UMAP. To integrate mouse and human samples while accounting for species-specific variation, reciprocal PCA (RPCA) integration was applied using Seurat. To further correct for batch effects across samples and experimental conditions, the integrated dataset was processed with Harmony,[117] after which dimensionality reduction was recalculated and clustering performed.

Cell-cell communication

To infer intercellular communication, we used CellChat v2 on the batch-corrected Seurat object.[118] The Secreted Signaling, Cell-Cell Contact, and ECM-Receptor database were subsetted and used for the analysis. Different experimental group datasets were analyzed independently, and the resulting CellChat objects were merged using the merge CellChat function to compare signaling networks. Visualization of inferred interactions and ligand–receptor pairs followed the guidelines provided in the CellChat vignette (https://github.com/jinworks/CellChat). Analyses were performed separately on human-only cells to characterize intra-species communication, and on integrated human–mouse datasets to investigate cross-species signaling following cross-species integration.

Immunofluorescence Staining

Whole-mount staining

The kidney progenitor assembloids were fixed in 4% PFA for 15 minutes in Eppendorf tubes at room temperature. They were then washed four times with 1X PBS (Corning, Cat. No. 21-040-CV) for total of 30 minutes. After the washes, these samples were blocked

with blocking buffer (0.3% PBST containing 2% BSA) for 30 minutes at room temperature or overnight at 4°C, followed by primary antibody staining (primary antibodies were diluted in blocking buffer) at 4°C overnight. On the next day, kidney progenitor assembloids were washed four times with 0.3% PBST for total of 30 minutes at room temperature, followed by secondary staining (secondary antibodies were diluted in blocking buffer) at 4°C overnight. Then, these kidney progenitor assembloids were washed again with 0.3% PBST for 30 minutes at room temperature and then mounted on a cover slip in Flouoromount-G (SouthernBiotech, Cat. No. 0100-01). The samples were imaged utilizing the Confocal Microscope (Zeiss LSM 800: AxioObserver.M2).

Staining on 96-well plates

For each well, culture medium was first removed and 50μl 4% PFA was added to fix the samples for 10 minutes at room temperature. These samples were then gently washed three times with 1X PBS (Corning, Cat. No. 21-040-CV) for total 15 minutes. After the washes, samples were blocked in 100μl blocking solution (0.3% PBST containing 2% BSA) for 30 minutes at room temperature, followed by primary antibody staining at room temperature for 2 hours. After the primary staining, samples were gently washed two times with PBST for total 10 minutes, followed by secondary staining at room temperature for one hour. Then, the samples were gently washed three times with PBST for total 15 minutes, and 100μl PBST was kept in the well after the final wash for imaging.

Staining with cryo-sections

i. OCT block generation for hKPA transplants. Dissected hKPA transplants were fixed with 4% PFA for 25 minutes, and then washed with PBS for 4-5 times to remove the residual PFA. After wash, hKPA transplants were transferred into 1.7mL tube containing 30% sucrose for 1 day at 4°C. When transplants sunk down at the bottom of tube, they were used for OCT (Scigen, Cat. No. 4586K1) cryo-block generation and making cryosection slides with Cryostat (Leica).

ii. Immunofluorescence staining with cryosection slides. Cryo-section slides were removed from -80°C freezer and incubated with PBS for 10 minutes to remove the OCT. After PBS wash, ImmEdge Hydrophobic Barrier PAP Pen was used to make a cycle surrounding the sample. Blocking solution (0.3% PBST containing 2% BSA) were added to cover the sample for 30 minutes incubation at room temperature. After blocking solution incubation, primary antibody solution was added to cover the sample for 1 hour at room temperature. After primary antibody solution incubation, sample was washed with PBST for 3-4 times followed by secondary antibody solution incubation for 1 hour at room temperature. After secondary antibody solution incubation, sample was washed with PBST for 4-5 times and then mounted with Fluoromount-G® Mounting Medium. The slides were ready for recording with fluorescence microscope.

RNAscope *in situ* hybridization

We utilized RNAscope™ Multiplex Fluorescent Reagent Kit v2 (Advanced Cell Diagnostics, Inc.) to perform fluorescence *in situ* hybridization on P5 mouse kidney frozen sections and whole-mount KPAs. **(1)** For fluorescence *in situ* hybridization on P5 mouse kidney frozen sections, cryosections (10 μm) were first treated with 4% PFA at 4°C for 2 hours, followed by standard pretreatment steps for fixed frozen tissue samples following the protocol, where samples were treated with hydrogen peroxide and protease. The pretreated samples were then hybridized with RNAscope probes for 2 hours at 40°C using the HybEZ oven (Advanced Cell Diagnostics, Inc.). The probes were then amplified and detected with tyramide signal amplification fluorescence. **(2)** For whole-mount KPAs, we referred to the ACD zebrafish whole-mount protocol. Briefly, KPAs were fixed with 4% PFA (Electron Microscopy Sciences, Cat # 157-4) for 24 hours at 4°C, then dehydrated with a series of methanol gradient treatment (25%, 50%, 75%, 100%). These dehydrated KPAs can be stored in 100% methanol in -20°C for up to two months. When ready to proceed for whole-mount staining, dehydrated kidney progenitor assembloids would be rehydrated through a reversed series of methanol gradient treatment (100%, 75%, 50%, 25%) and kept in 1X PBST containing 1% BSA at room temperature. Next, these KPAs were treated with 1X Target Retrieval solution for 15 minutes, changed back to 1X PBST containing 1% BSA, washed with 100% methanol for 1 min, then transferred into 0.2 mL PCR tube and washed with 1X PBST containing 1% BSA. After carefully removing 1X PBST containing 1% BSA as much as possible without letting the samples completely dry, 300 μL of Protease Plus was added into the tube and incubated at 40°C for 30 mins. The tube was placed horizontally floating in a water bath. After the incubation, Protease Plus was replaced with 300 μL of Probe Diluent. Next, typical Probe Hybridization and Staining with RNAscope™ Multiplex Fluorescent Reagent Kit v2 were performed after removing the Probe Diluent from the tube. Antibody-based Immunofluorescence staining was performed following the Probe Hybridization and Staining. The catalog numbers of probes from Advanced Cell Diagnostics, Inc. used in this work are listed as follow: *Igfbp6* (425721-C1), *Alx1* (403161-C3), and *Penk* (318761-C3). RNAscope® Assay on Whole Zebrafish Embryos was described in detail at the link https://acdbio.com/sites/default/files/MK%2050-016%20Zebrafish_WISH_Tech%20Note_12042017.pdf

TUNEL assay

Whole hKPAs grown *in vitro* or cryosection slides of hKPAs grown *in vivo* were stained using the Click-iT Plus TUNEL Assay kit (Invitrogen, Cat# C10617) following the manufacturer's instructions. Briefly, cryosection slides were incubated with the TdT reaction buffer for 10 min at 37°C in 1.5mL Eppendorf tube or on the slide. TdT reaction buffer was then removed and replaced by TdT reaction mixture and incubated for 1 hour at 37°C. After the 1-hour incubation, TdT reaction mixture was removed, and the samples were rinsed with PBST (0.3% Triton X-100 in PBS). Next, the samples were incubated with the Click-iT Plus TUNEL reaction cocktail at 37°C for 30 minutes in dark, followed by PBST washes and immunofluorescence staining as detailed above.

RNA isolation, reverse transcription and RT-qPCR

Samples were dissolved in 100μl TRIzol (Invitrogen, Cat. No. 15596018) or 100 μl DNA/RNA Shield (Zymo Research, Cat. No. R1100-50) and kept in -80°C freezer. RNA isolation was performed using the Direct-zol RNA MicroPrep Kit (Zymo Research, Cat. No. R2062) or Quick-RNA Microprep Kit (Zymo Research, Cat. No. R1051) according to the manufacturer's instructions. Reverse transcription was performed using the iScript Reverse Transcription Supermix (Bio-Rad, Cat. No. 1708841) following the manufacturer's instructions. RT-qPCR was performed using the Ssoadvanced™ Universal SYBR (Bio-Rad, Cat# 1725274) or AzuraView GreenFast qPCR Blue Mix LR (Azura Genomics, Cat# AZ-2320) and carried out on an Applied Biosystems Vii 7 RT-PCR system (Life Technologies). Validated gene-specific primers can be found in Methods S5. Fold change was calculated from ΔCt using *Gapdh* as housekeeping gene as previously described.[119]

QUANTIFICATION AND STATISTICAL ANALYSIS

For immunostaining quantification, 3-4 different fields of view were randomly selected to count the number of positively-stained cells and total cell numbers. At least 500 cells in total were counted from each field of view. Error bars represent standard derivation between different fields of views. ImageJ (version: 2.1.0) software was applied to quantify the intensity of targeted fluorescence signals (n=6 areas), thickness of myofibroblast layer surrounding the $PKD2^{-/-}$ hKPAs transplant cysts or wildtype hKPAs transplant tubules (n=6 cysts or tubules), distance of macrophages to the closest cyst or tubule (n=4 cysts or tubules), area of renal vesicle in D5 hKPA (n=15 renal vesicles/group). Olympus Cellsens Standard software was applied to measure the area of $PKD2^{-/-}$ hKPAs transplant cysts or wildtype hKPAs transplant lumens (n=14 cysts or lumens). For quantification of the number of nephrogenic niches, we define one nephrogenic niche as a structure with a UB budding tip, capped sequentially by $SIX2^{+}$ NPCs and $FOXD1^{+}$ IPCs.